Czech Technical University in Prague
Faculty of Nuclear Sciences and Physical Engineering

Department of Physics

Quarkonia studies using the ATLAS detector at the LHC

Bachelor Thesis

Radek Novotný
Supervisor: Ing. Michal Marčišovský
Prague, 2014

České vysoké učení technické v Praze

Fakulta jaderná a fyzikálně inženýrská

Katedra Fyziky

Studium kvarkonií na urychlovači LHC pomocí detektoru ATLAS

Bakalářská práce

Radek Novotný

Vedoucí práce: Ing. Michal Marčišovský

Praha, 2014

Declaration

I hereby declare that this thesis is the result of my own work and all the sources I used are in the list of references.

I have no objection to usage of this work in compliance with the act §60 Law No. 121/2000 Coll. (Copyright Act), and with the rights connected with the copyright act including the changes in the act.

Prohlášení

Prohlašuji, že jsem svou bakalářskou práci vypracoval samostatně a použil jsem pouze podklady uvedené v přiloženém seznamu.

Nemám závažný důvod proti použití tohoto školního díla ve smyslu §60 Zánona č. 121/2000 Sb., o právu autorském, o právech souvisejících s právem autorským a o změně některých zákonů (autorský zákon).

V Praze dne ....

Radek Novotný

Acknowledgement

Foremost, I would like to thank to my supervisor, Michal Marčišovský for his professional guidance, patience, willingness and invaluable advice. I would also like to thank Mária Čarná for her carefully reading of the manuscript and Václav Vrba for overall support of my work. I am also grateful to the classmates for their academic support. Last but not least I would like to thank my family and friends for the continuous support they have given me during my studies.

Radek Novotný

Title: **Quarkonia studies using the ATLAS detector at the LHC**

Author: Radek Novotný

Field of study: Nuclear Engineering

Specialization: Experimental Nuclear and Particle Physics

Sort of project: Bachelor thesis

Supervisor: Ing. Michal Marčišovský

Abstract:

The quarkonium is bound state of a heavy quark and antiquark of the same flavour. It is the simplest system bound by a combination of strong and electromagnetic interactions. Since the binding energies of the quarkonia systems are at the edge of perturbative QCD energy scale, study of the $Q\bar{Q}$ system properties serves to improve the understanding of the strong force. The most widely known state of charmonium is the J/ψ resonance, which can decay via electromagnetic interaction into a $\mu^+\mu^-$ or e^+e^- pair, easily observed in detector. This thesis is devoted to the measurement of the double-differential inclusive fiducial $J/\psi \rightarrow \mu^+\mu^-$ production cross section in proton-proton collisions measured by the ATLAS detector at the Large Hadron Collider (LHC). Furthermore, the measurement of fraction of J/ψ produced indirectly from the decay of B mesons is presented.

In the beginning of this thesis, the Standard Model of particles and interactions, the ATLAS experiment and the elementary properties of the J/ψ resonance are briefly introduced. In the following chapters, the analysis procedure, results and comparison with the Monte Carlo samples are presented.

Key words: J/ψ, quarkonia, ATLAS, LHC, Standard Model, non-prompt production

Název práce: **Studium kvarkonií na urychlovači LHC pomocí detektoru ATLAS**

Autor: Radek Novotný

Obor studia: Jaderné inženýrství

Zaměření: Experimentální Jaderná a Částicová Fyzika

Druh práce: Bakalářská práce

Vedoucí práce: Ing. Michal Marčišovský

Abstrakt:

Kvaronium je vázaná stav těžkého kvarku a příslušného antikvarku stejné vůně. Jakožto nejjednodušší systémem svázaný silnou interakcí, slouží ke studiu vlastností této síly. Jedním ze zástupců kvarkonií je charmonium skládající se z charm kvarku a antikvarku. Základním stavem charmonia je dobře známá rezonance J/ψ, která se může rozpadat pomocí slabé interakce například na $\mu^+\mu^-$ nebo e^+e^-.

Tato práce se zabývá se měřením diferenciálního účinného průřezu při inkluzivní produkci $J/\psi \to \mu^+\mu^-$ určované na citlivé oblasti detektoru ATLAS. Detektor ATLAS se nachází na velkém hadronovém urychlovači LHC v laboratoři CERN a pro účel této práce byly použity pouze data z proton-protonových srážek. Tato práce se dále zabývá měřením podílu J/ψ vyprodukovaných z rozpadu B mezonů.

Úvodní část této práce se věnuje základnímu popisu Standardního modelu a experimentu ATLAS. Dále jsou uvedeny stručné informace o J/ψ rezonanci, historie jejího objevu a současný stav výzkumu v této oblasti. V poslední části je popsán proces, jakým jsou data zpracována. Závěrem této práce jsou prezentovány výsledky měření a porovnání reálných dat s Monte Carlo simulacemi.

Klíčová slova: J/ψ, kvarkonia, ATLAS, LHC, Standardní Model, nepřímá produkce

Contents

Chapter 1

Introduction to the subatomic physics

The subatomic physics deals with interactions at a scale smaller than 1 fm. It takes into account the laws of quantum mechanics and Einstein's special theory of relativity. Because there is no unified theory of all known interactions, it has to make a compromise between them. In many cases, such as heavy quarkonia, the relativistic effect can be neglected. This paragraph describes some important relations which will be used in this thesis.

1.1 The parity and charge conjugation invariance

The wave function ψ describes state of the elementary particles. The parity operator acts on wave function ψ, which can be for a non-relativistic spinless particle a solution to the Schrödinger wave equation,

$$-i\hbar\frac{\partial}{\partial t}\psi = \frac{1}{2m}\nabla^2\psi. \tag{1.1}$$

The parity is an operation of the spatial inversion of the coordinate system $(x,\ y,\ z,\ t \rightarrow -x,\ -y,\ -z,\ t)$. This is an example of discrete transformation which is produced by the parity operator $\hat{\mathrm{P}}$.

$$\hat{P}\psi(r) = \psi(-r) \tag{1.2}$$

The eigenvalues of parity operator are ± 1. Thus, a wave function can be classified by parity, which can be even (P = +1), or odd (P = -1).

The charge conjugation operator $\hat{\mathrm{C}}$ reverses the sign of the charge and magnetic momentum of particle's wave function. For fundamental particles, it is equal to the interchange of particle and its corresponding antiparticle. Similar to parity, it is an unitary discrete transformation with eigenvalues ± 1 and can define a wave function behavior.

Strong and electromagnetic interactions are found experimentally to be invariant under the parity and charge conjugation invariance, but both symmetries are broken in weak interactions. That is why the CP symmetry, the combination of parity and charge conjugation symmetry, was introduced. For a long time, it was thought that the CP symmetry is conserved in the weak interaction, but in 1964 Christenson *et al.* [1] discovered that in the neutral kaon decays this invariance is also broken. [2]

The time reversal operator $\hat{\mathrm{T}}$ simply inverts the time coordinates $(t \rightarrow -t)$. At present, it is expected, that all interactions are invariant under the combination of the C, P, T transformations, often called CPT theorem. The CPT invariance and the violation of CP symmetry implies the violation of T symmetry. The violation of T symmetry may be the reason of dominance of the matter over antimatter.

1.2 Standard model

Particle physics is dealing with the particles that are the constituents of what is usually referred to as matter and radiation. There were many models trying to describe well known phenomena and physical laws. In the 1970s, the Standard Model (SM) of particles and their interactions was formed. This model is in best agreement with experimental data. The Standard Model assumes, that our world is made of 17 elementary particles. The first group is called fermions and has a half-integer spin. The second group is called bosons and has an integer spin. The particles interact via four known types of forces: electromagnetic, strong, weak and gravitational which latter not being part of the SM. The complete list of elementary particles and some of their properties is shown in Tab. 1.1.

	Symbol	Name	Mass	Electric charge	Spin
Quarks	u	up	$2.3^{+0.7}_{-0.5}$ MeV	2/3	1/2
	d	down	$4.8^{+0.5}_{-0.3}$ MeV	-1/3	1/2
	s	strange	95±5 MeV	-1/3	1/2
	c	charm	1.275±0.025 GeV	2/3	1/2
	b	bottom	4.18±0.03 GeV	-1/3	1/2
	t	top	173.07±0.52±0.72 GeV	2/3	1/2
Leptons	e	electron	0.510998928±0.000000011 MeV	-1	1/2
	μ	muon	105.6583715±0.0000035 MeV	-1	1/2
	τ	tau	1776.82±0.16 MeV	-1	1/2
	ν_e	e-neutrino	< 2 eV	0	1/2
	ν_μ	μ-neutrino	< 0.19 MeV	0	1/2
	ν_τ	τ-neutrino	< 18.2 MeV	0	1/2
Gauge bosons	γ	photon	0	0	1
	W^{+-}	W	80.385±0.015 GeV	±1	1
	Z	Z	91.1876±0.0021 GeV	0	1
	g	gluon	0	0	1
	H	Higgs	125.9±0.4 GeV	0	0 [3]

Table 1.1: The list of particles in the Standard Model. [4]

1.2.1 The interactions

Interactions in the Standard Model are realized as an exchange of mediating bosons, characteristic to the type of interaction between its constituents. Due to their character, they are frequently called exchange interactions.

Electromagnetic interaction is mediated by a massless photon and it has infinite range. This interaction acts between charged particles, and it is responsible for virtually all phenomena in extra-nuclear physics. Due to this interaction, electrons are bound to nucleus. The theory describing the electromagnetic interaction is called quantum electrodynamics (QED) and it later laid the ground of the quantum field theory (QFT), the framework for description of other interactions in the Standard Model.

Strong interaction binds quarks together in hadrons and is mediated by the exchange of massless gluons. Strong force is the strongest force compared to other forces, and its range is limited to 1 fm.

Weak interaction is responsible for the relatively slow processes of β decay. The mediators of this interaction are $W^{\pm}$ and Z^0 bosons. It is characterised by long lifetimes and small cross sections.

Gravitational interaction acts between all particles. Gravitational force is the weakest of all fundamental forces, and is almost 10^{-38} times weaker than strong interaction. Due to this fact, gravitational interaction is neglected in the SM. In the some particle theories, this interaction is mediated by a hypothetical particle graviton with spin 2.

1.2.2 Quarks

In the 1960s, M. Gell-Mann [5] and G. Zweig [6] were studying regularities between the lowest lying states of mesons and baryons which were then known. They built a model with an assumption that mesons and baryons are made of u, d and s quarks. The mesons are composed from two quarks and baryons are composed from three quarks. Quarks were simple mathematical objects which described hadrons rather than real physical objects. This model assumes an approximate $SU(3)$ flavour symmetry. The breaking of this symmetry is due to different masses of quarks. Figure 1.1 indicates the different meson states which were obtained from the composition of $SU(3)$ elements. For both (a) and (b), octet and singlet states can be observed. Mixing between octet and singlet must be assumed due to breaking of $SU(3)$ symmetry.

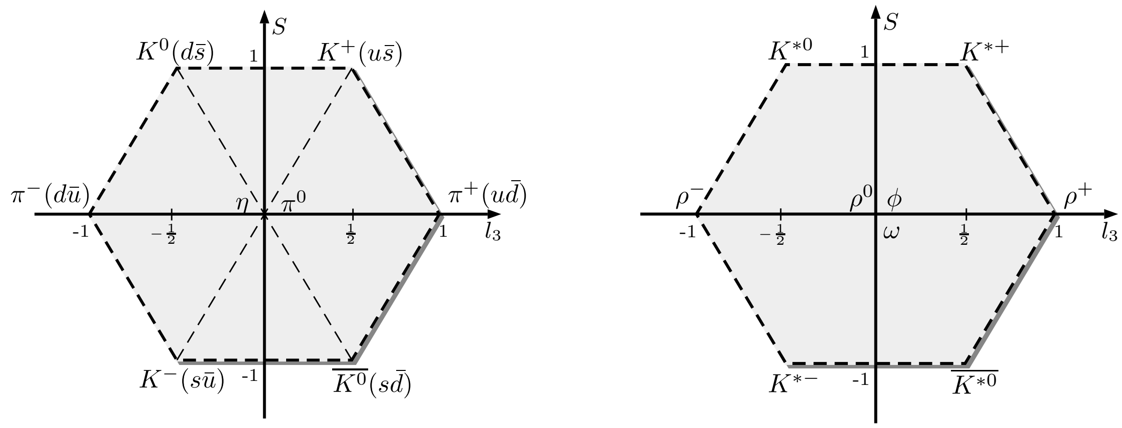

(a) The pseudoscalar meson states ($J^P = 0^-$)

(b) The vector meson states ($J^P = 1^-$)

Figure 1.1: The lowest lying meson states.

Six quarks are known at present, as can be seen in table 1.1. The quarks exist in three generations. Almost all matter around us is made of u and d quarks, which belong to the first generation. In the 1960s, new particles were observed which decay slower than was expected. To this particles was assigned an additional quantum number S called strangeness. After observation of c, b and t quarks, additional quantum numbers (charm, beauty and top) were assigned to baryons which carry these quarks. The first three quarks are referred to as light quarks q and the other three quarks are referred to as heavy quarks Q.

Tetraquark candidate

There are several candidates for particles which do not fit within standard hadron classification into mesons and baryons. The most known examples are the $X(3872)$ and $Z(4430)^-$ resonances. In 2007, the Belle collaboration announced the observation of new resonant state called $Z(4430)^-$. In 2014, the LHCb collaboration confirmed observation of this resonant state. This exotic particle can not be classified within the traditional quark model. Thus, this new resonant state became a possible candidate to be a tetraquark composed of $c\bar{c}d\bar{u}$ quarks. [7]

1.2.3 Leptons

At present, six leptons are known, which are similarly to quarks categorized into three generations. There are three charged leptons and to each of them there is a neutral neutrino. The masses or mass limits of leptons are given in table 1.1.

Neutrinos are specific with masses small in comparison to the corresponding charged leptons. Although the neutrinos have mass, in the Standard Model they are assumed to be massless. The neutrinos are also unique in that only negative projection of total angular momentum onto z axis was observed. This corresponds to pure helicity [1] state $H = -1$ (left-handed). The latest measurement of the Planck detector provides the upper limit for sum of the neutrino masses m_{ν_i} [8]

$$\sum_i m_{\nu_i} < 0.25 \text{ eV}. \tag{1.3}$$

1.2.4 Antiparticles

In 1928, British physicist Paul Adrien Maurice Dirac [9] derived the equation that combined quantum theory and special relativity to describe the behavior of an electron moving at a relativistic speed. The solution of this equation posed a problem with the existence of the negative energy states of electron. This negative states were interpreted as antiparticles, i.e. particles with same mass and lifetime as a corresponding particle, but with opposite charge and magnetic moment.

The existence of antiparticles is a general property of both fermions and bosons. The first observed antiparticle was the antiparticle of an electron, which is called positron. Due to the conservation laws, fermions must be created and destroyed in pairs. This mechanism is called pair-production and annihilation. For example, a γ-ray in the presence of nucleus can produce an electron-positron pair and materialize into e^+e^- bound state called positronium. This state annihilates into two or three γ-rays.

1.3 Weak interaction

1.3.1 Fermi theory

Enrico Fermi, an italian physicist, studied the properties of β-decay and he made the first step in the description of the weak interaction using the apparatus of the QFT. Because weak interaction acts on short distances (10^{-2} fm), he imagined a point-like interaction of four fermions coupled by a Fermi weak coupling constant G_{F}. The Fermi model is valid only for the low momentum transfer region of phase space, and breaks down at high energies. The weak interaction lagrangian was described by the product of a weak current, J^λ, with its hermitian conjugate

$$\mathcal{L} = \frac{G_F}{\sqrt{2}} J^\lambda J_\lambda^\dagger. \tag{1.4}$$

[1] Helicity is the projection of the spin $\vec{S}$ onto the direction of momentum $\vec{p}$. [2]

This theory of weak interactions proposed by Fermi had to be modified after the discovery of parity violation in the weak interaction by T.D. Lee, C.N. Yang [10] and C.S. Wu [11] in 1956 and 1957, respectively. The Fermi's vector current was replaced by an mixture of vector (V) and axial vector (A) currents. Thus, Fermi's theory is often called V-A theory.

We now know, that the weak interaction is mediated by three massive gauge bosons and Fermi coupling takes the following form

$$G_{\mathrm{F}} = \frac{g^2}{M_{\mathrm{W}}^2}, \tag{1.5}$$

with g being the weak charge and M_{W} the mass of a W boson. Since the W boson is very heavy, the weak interaction acts on short distances and the decay times are longer compared to other interactions.

1.3.2 Cabibbo theorem

Cabibbo studied the weak decay of strange particles (particles containing s quarks) and he realized that d quark is not an eigenstate of the weak interaction. The weak interaction acts instead on a rotated state composed of d and s quarks

$$d_C = d \cdot \cos\theta_C + s \cdot \sin\theta_C, \tag{1.6}$$

where the mixing angle θ_C is called a Cabibbo angle. This rotation causes the weak coupling G for $\Delta S = 0$ decay [2] to be effectively $G \cdot \cos\theta_C$ and for $\Delta S = 1$ decay it is $G \cdot \sin\theta_C$. The Cabibbo angle can be determined from an experiment by measuring the ratio between $\Gamma(K^+ \to \mu\nu)$ and $\Gamma(\pi^+ \to \mu\nu)$ [12]. This gives a result of $\theta_C \simeq 13°$.

1.3.3 The GIM mechanism and CKM matrix

In 1970, Glashow, Iliopoulos and Maiani (GIM) [13] proposed a new quark, later called charm, to solve the puzzle of the high predicted rates of $K^0 \to \mu^+\mu^-$ transition, which were not observed in experiments. The introduction of fourth quark led to a symmetry between quarks and four then known leptons. The interference between the possible decay channels lowered the predicted cross-sections to be compatible with the observed rates. The new quark is coupled by the weak interaction to the superposition of d and s quarks orthogonal to the Cabibbo combination d_C, equation 1.6.

$$s_C = -d \cdot \sin\theta_C + s \cdot \cos\theta_C. \tag{1.7}$$

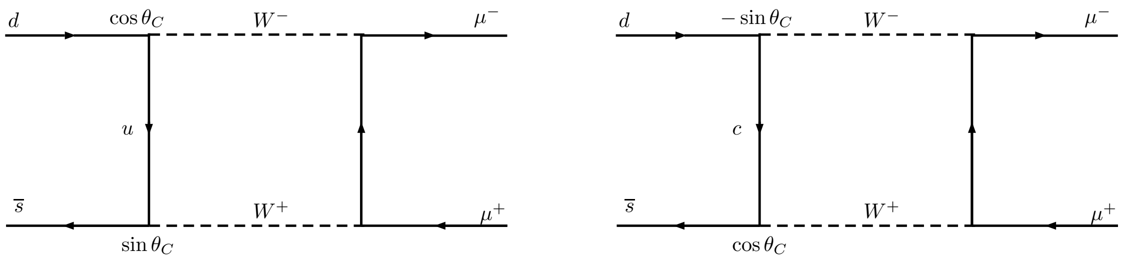

Figure 1.2: Feynman diagram for $K^0 \to \mu^+\mu^-$. [14]

For each up quark exchanged, the charm quark provides a second diagram with a coupling of opposite sign. In fact, if the mass of the charmed quark was equal to the mass of the up quark, the two diagrams would cancel each other. For unequal masses, the result must be proportional to the difference $m_c^2 - m_u^2$.

[2] ΔS is the change of strangeness between initial and final state.

Because the transition occurs, the new quark must have larger mass and from the predictions of Ioffe and Shabalin, the mass of charm quark should be in range of $1.5 - 2$ GeV. Including these results, the four quarks can be described by an approximate $SU(4)$ symmetry which is violated more due to heavy charm quark than the previous $SU(3)$ flavour symmetry with three quarks.

The GIM mechanism can be extended to all six known quarks. The quark mixing can be described by the unitary transformation,

$$\begin{pmatrix} d' \\ s' \\ b' \end{pmatrix} = \begin{pmatrix} V_{ud} & V_{us} & V_{ub} \\ V_{cd} & V_{cs} & V_{cb} \\ V_{td} & V_{ts} & V_{tb} \end{pmatrix} \begin{pmatrix} d \\ s \\ b \end{pmatrix} \tag{1.8}$$

where the matrix is called CKM matrix (after Cabibbo, Kobayashi and Maskawa). Each matrix element can be assigned to a particular vertex in the Feynman diagram and modify decay amplitude. This implies that some processes allowed before are suppressed by the CKM mechanism, for instance previously mentioned $K^0 \to \mu^+\mu^-$. Furthermore, the CKM matrix can be parametrized by three angles and a phase, which is the only source of CP violation in the SM.

1.4 Strong interaction

1.4.1 Colour

The colour is an additional internal degree of freedom of quarks. This degree of freedom was introduced after the observation of Δ^{++} baryon which is made of three up quarks. This baryon will break the Pauli exclusion principle without introduction of another degree of freedom, called colour charge. Thus, there are three colors red, green and blue with their respective anticolours. As mentioned above, strong interaction is mediated by an exchange of massless gluons. These gluons carry colour and anticolour charge and provide colour interaction between two quarks. With three colours and three anticolours, there is a coloured gluon octet with possible combinations taking form of

$$r\bar{b},\ r\bar{g},\ b\bar{g},\ b\bar{r},\ g\bar{r},\ g\bar{b},\ \frac{1}{\sqrt{2}}(r\bar{r} - b\bar{b}),\ \frac{1}{\sqrt{6}}(r\bar{r} + b\bar{b} - 2g\bar{g}), \tag{1.9}$$

and a colourless gluon singlet $\frac{1}{\sqrt{3}}(r\bar{r} + b\bar{b} + g\bar{g})$.

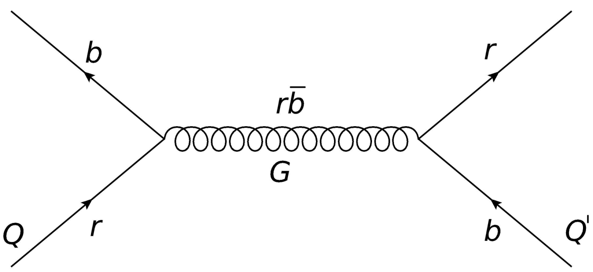

Figure 1.3: QQ' interaction via coloured gluon exchange. The time runs from bottom to top.

The colour charge of the strong interaction is analogous to the electric charge in electromagnetic interaction. Both forces are mediated by massless vector particles, but compared to photons, gluons can interact with each other. This phenomena is called gluon self coupling. Due to gluon self coupling, the colour charge exhibits a particular behavior called antiscreening. It is the opposite to the screening of electric charge in QED.

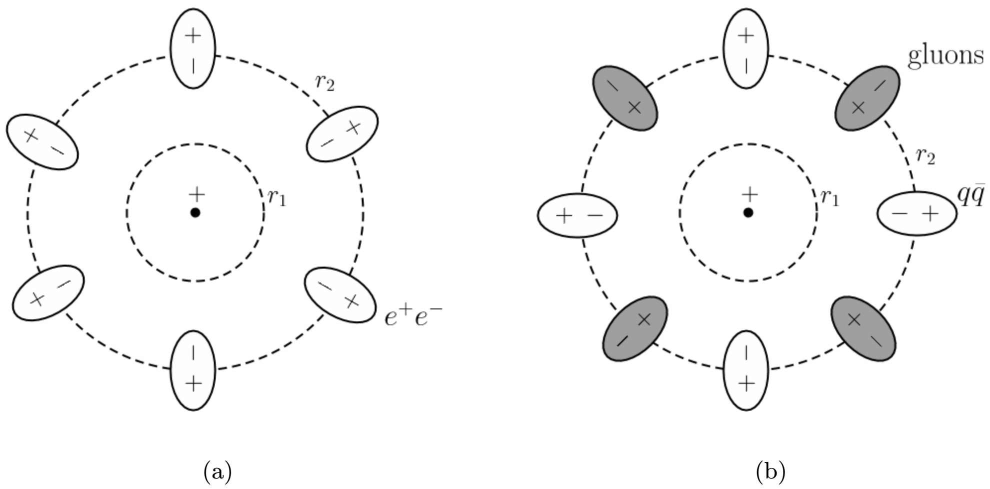

Figure 1.4: Screening of electric charge by virtual electron-positron pairs in (a) and antiscreening of the colour charge by gluons and screening by quarks in (b). [15]

Both baryons and mesons must be colourless, thus the quarks and gluons are confined inside hadrons. No free quarks were observed , with the exception of the top quark, which decays before it has a chance to hadronize.

1.4.2 QCD

The theory describing the interactions between quarks and gluons based on a colour exchange is called quantum chromodynamics (QCD). Despite photons and gluons being massless, the QCD potential takes a different form due to the differences between those forces. The simplest potential model for mesons that describes strong interaction is called Cornell potential model and it takes form

$$V_s(r) = -\frac{4}{3}\frac{\alpha_s}{r} + kr, \tag{1.10}$$

where α_s is the strong interaction coupling and k is a free parameter. The first part of the equation is similar to the Coulomb potential with a factor of $\frac{4}{3}$. This factor arises from eight colour gluon states averaged over three quark colours. The factor is divided by 2 from the definition of α_s. The second, linear term is associated with colour confinement at large r.

The Cornell potential can be extended by inclusion of the spin interaction between quarks. These spin-dependent potentials are assumed to be dominated by a one-gluon exchange and consist of spin-spin, tensor and spin-orbit terms. For a system of two quarks, the potential takes the following form [16]:

$$V_{q\bar{q}} = -\frac{4}{3}\frac{\alpha_s}{r} + \sigma r + \frac{32\pi\alpha_s}{9m_q^2}\delta(r)\mathbf{S}_q \cdot \mathbf{S}_{\bar{q}} + \frac{1}{m_q^2}\left[\left(\frac{2\alpha_s}{r^3} - \frac{b}{2r}\right)\mathbf{L}\cdot\mathbf{S} + \frac{4\alpha_s}{r^3}\mathbf{T}\right], \tag{1.11}$$

where the $\mathbf{L}$ is an orbital momentum, $\mathbf{S}_q$ is a spin momentum of a particular quark, $\mathbf{S} = \mathbf{S}_q + \mathbf{S}_{\bar{q}}$ and $\mathbf{T}$ is a tensor term.

These extended models give better results, but still they are not satisfactory. Thus, the new interquark potential models are being developed and tested.

1.4.3 Running coupling

Charge screening in the QED (screening) and QCD (antiscreening) leads to the concept of a running coupling (the energy dependence of a strong coupling). In the QED, the coupling becomes large at (very) short distance and large energies, but its effect is small. In the QCD, the antiscreening effect causes the strong coupling to become small at short distance (large momentum transfer). This causes the quarks inside hadrons to behave more or less like free particles. This property of the strong interaction is called asymptotic freedom.

On the other hand, at the increasing distance, the coupling becomes so strong that it is impossible to isolate a quark from a hadron. In addition, if the quark pair receives more energy than is necessary for the production of a new quark antiquark pair, then it is energetically favourable to produce a new quark pair. This mechanism is called colour confinement.

Using perturbative QCD (pQCD) calculations and experimental data, the coupling constant of the QCD can be shown to have the following energy scale-dependence

$$\alpha_s(Q) = \frac{2\pi}{\beta_0 \ln \frac{Q}{\Lambda_{\mathrm{QCD}}}}, \tag{1.12}$$

where $\beta_0 = 11 - \frac{2}{3}n_f$, with n_f being the number of the active quark flavor, and Λ_{QCD} is the QCD scale [4]. The value of $\Lambda_{\mathrm{QCD}} = (0.339 \pm 0.010)$ GeV is determined by experiments. This dependence is valid only for $Q^2 \gg 2\Lambda^2$, where the Q is transferred momentum. The summary of measurements of $\alpha_s(Q)$ from multiple experiments is shown in Figure 1.5.

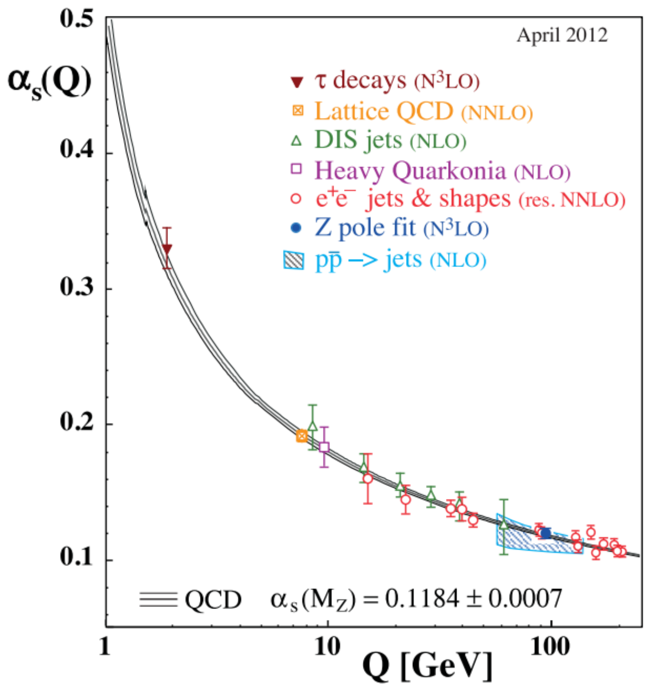

Figure 1.5: Summary of measurements of $\alpha_s(Q)$ as a function of the respective energy scale Q. The respective degree of the QCD perturbation theory used in the extraction of α_s is indicated in brackets (NLO: next-to-leading order; NNLO: next-to-next-to leading order; res. NNLO: NNLO matched with resummed next-to-leading logs; N^{3}LO: next-to-NNLO)^3. [4]

1.4.4 OZI rule

From the laws of strong interaction, the so-called OZI rule for decays follows. The Okubo-Zweig-Iizuka rule asserts that the processes with disconnected quark line diagrams are suppressed. Starting as a phenomenological interpretation of e.g. a large branching fraction of φ decays into $K\bar{K}$ final states, the OZI rule found its basis in the QCD framework. Despite being based on a very simplistic picture, the OZI prediction is fulfilled in most types of reactions, but the numerous reported violations of the OZI rule show that the underlying physics is more complicated. In the figure 1.6, the example of the OZI suppressed decay can be seen. [17]

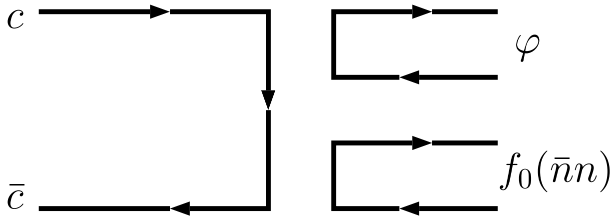

Figure 1.6: The OZI-forbidden decay.

1.5 Luminosity

Luminosity ($\mathcal{L}$) [18] is one of the most important parameters of an collider besides it's center-of-mass energy ($\mathrm{E_{CMS}}$). It is a measure of the number of collisions that are produced in a detector per cm squared and per second. In case of two colliding bunches of particles, the luminosity is defined as

$$\mathcal{L} = f\frac{n_1 n_2}{4\pi\sigma_x\sigma_y}, \tag{1.13}$$

where n_1, n_2 is the number of particles in bunches, f is frequency of collisions and σ_x, σ_y characterize the Gaussian transverse beam profiles in the horizontal and vertical directions. To simplify the expression, it is assumed that the bunches are identical in the transverse profile, that the profiles are independent of position along the bunch, and that the particle distributions are not altered during collision.

The integrated luminosity, or also called accumulated statistics, is important, because it shows how many physical events with cross-section σ can be observed per sample of data,

$$N_{\mathrm{Exp}} = \sigma_{\mathrm{Exp}}\int \mathcal{L}(r)dr, \tag{1.14}$$

where $\mathrm{N_{Exp}}$ is the number of events and σ_{Exp} is the interaction cross-section.

1.6 The cross-section and reaction rate

The interaction cross-section σ is equal to the effective area of interaction. If we consider a process with reaction rate W(the number of particles produced per second), the interaction cross-section can be written as

$$\sigma = \frac{W}{\mathcal{L}}, \tag{1.15}$$

[3]NLO etc. are the levels of the perturbation QCD theory into which the Feynman diagrams are counted.

where $\mathcal{L}$ is luminosity. The unit of cross-section is defined as barn: $1\ b = 10^{-28}\ \mathrm{m}^2$.

The reaction rate W can also be obtained from the perturbation theory (Fermi's Second Golden Rule) [2]

$$W = \frac{2\pi}{\hbar}|M_{if}|^2\rho_f. \tag{1.16}$$

The M_{if} is the matrix element between initial and final states, ρ_f is the energy density.

Since detectors do not cover a full solid angle around the interaction point, the differential cross-section is used. Differential cross-section is defined as

$$d\sigma(\theta) = \frac{N(\theta)d\Omega}{N_0}, \tag{1.17}$$

where $N(\theta)\ d\Omega$ is the number of particles passing every second through the element of solid angle $d\Omega$ and N_0 is the number of particles per cm^2 and second.

1.7 Decays and resonances

The mean lifetime of decaying state is defined as $\tau = 1/W$, with total width W defined in chapter 1.6. In particle physics, where the lifetimes are usually short, the width of resonance Γ is frequently used. The Γ is defined as

$$\Gamma = \frac{\hbar}{\tau} = \hbar W = 2\pi|M|^2\int\rho_f d\Omega. \tag{1.18}$$

The lifetime is related to the width by the uncertainty principle, $\Delta E\Delta t \geq \hbar$.

The states with finite widths and lifetimes are referred to as resonances. The resonance can decay in general via several different channels and the total width is a sum of the partial widths. The following relation is called branching ratio, and it describes the fraction of decays in one particular channel i to all possible decay channels.

$$Br_i = \frac{\Gamma_i}{\Gamma_{\mathrm{tot}}}. \tag{1.19}$$

The shape of the resonance peak (the energy dependence of cross-section) is described by the Breit-Wiegner distribution

$$\sigma(E) = \sigma_{\max}\frac{\Gamma^2/4}{(E-E_R)^2+\Gamma^2/4}, \tag{1.20}$$

where E_R is the central value of energy, $\sigma_{\max}$ is the maximum amplitude and Γ is the total width of resonance.

The Z^0 boson is an example of a resonance which can decay via multiple channels, e.g. into $\mathcal{Q}\bar{\mathcal{Q}}$, $\mu^+\mu^-$, hadrons or neutrino pairs. The total width of Z^0 is Γ_{tot}, partial widths $Z^0 \to$ hadrons and $Z^0 \to l^+l^-$ denote Γ_{h} and Γ_{l}. The width of invisible decays into N_ν, light neutrino species can be calculated as

$$\Gamma_{\mathrm{inv}} = \Gamma_{\mathrm{tot}} - \Gamma_{\mathrm{h}} - 3\Gamma_{\mathrm{l}}. \tag{1.21}$$

The ratio of neutrino and charged leptonic partial widths $(\Gamma_\nu/\Gamma_{\mathrm{l}})_{\mathrm{SM}}$ is predicted by the Standard Model. To determine the number of light neutrino species, one needs to calculate

$$N_\nu = \frac{\Gamma_{\mathrm{inv}}}{\Gamma_{\mathrm{l}}}\left(\frac{\Gamma_{\mathrm{l}}}{\Gamma_\nu}\right)_{\mathrm{SM}}. \tag{1.22}$$

The cross-section of $Z^0 \to$ hadrons with a dependence on the number of light neutrino types is shown in Figure 1.7.

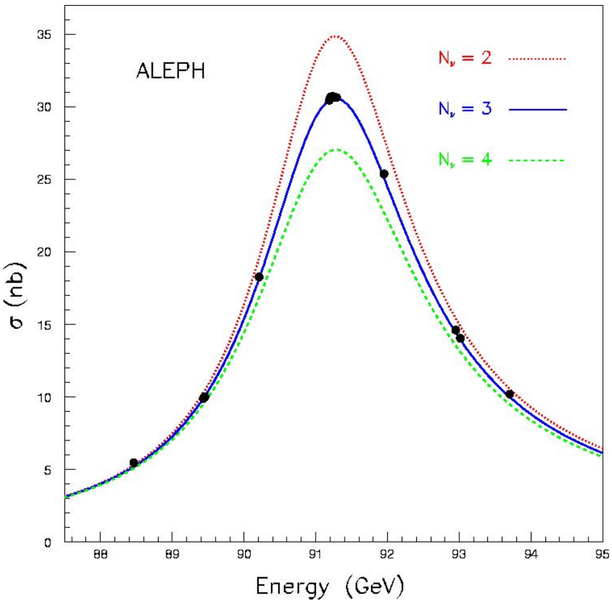

Figure 1.7: The cross-section for the reaction $e^+e^- \rightarrow Z^0 \rightarrow$ hadrons in the invariant mass range of the Z^0. The three curves are theoretical predictions dependent on the number of neutrino flavours. Experimental measurements are represented as dots and clearly fit the three neutrino case. [19]

Chapter 2

The LHC and the ATLAS detector

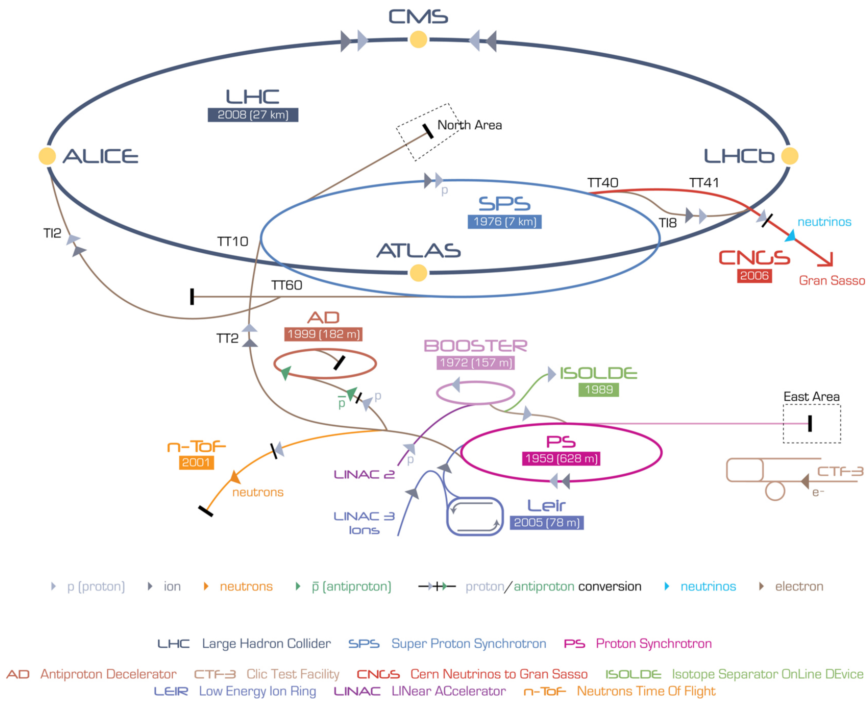

Figure 2.1: The LHC Complex. The protons are accelerated gradually in the accelerator chain. The first step in the chain is linear accelerator Linac2. The Linac2 accelerates protons to 50 MeV. The second step is the Proton Synchrotron Booster (PSB), which accelerates the protons to 1.4 GeV. Its role besides acceleration is to increase the luminosity of the proton beam. The beam is then injected into the Proton Synchrotron (PS), which accelerates the beam to 25 GeV. Protons are then sent to the Super Proton Synchrotron (SPS), where they are accelerated to 450 GeV. Then the protons are finally injected into two beampipes of the LHC, where the protons are accelerated up to 4 TeV per beam (2012) and after the first long shutdown (2013-2014) up to 6.5 TeV, which is close to the nominal LHC energy $(7 + 7)$ TeV. The LHC is also able to accelerate Pb^{208} ions which start their journey at the Linac3 linear accelerator, and after accumulation in the Leir storage ring, they are injected into the PS. The acceleration process is the same as for protons, but the nominal energy is different. [20] [21]

At present, the LHC (Large Hadron Collider) is the largest particle accelerator and it is located in the CERN laboratory near Geneva, Switzerland. The LHC provides high luminosity high energy beams and opens doors to new kinematic regions. The LHC is designed to provide bunches of 10^{11} protons which collide with frequency of 40 MHz. It also provides lead ion beams with bunches containing 7×10^{7} Pb^{208} ions. The design luminosity for protons is 10^{34} cm^{-2}s^{-1}. The LHC complex houses several particle physics experiments. The largest are ATLAS, CMS, ALICE and LHCb. The rest of the experiments can be found in [22].

2.1 The ATLAS detector

The ATLAS (A Toroidal LHC ApparatuS) detector is designed for exploration of new physics in p-p collisions at 14 TeV center of mass energy. Its main purpose is to study the Standard Model, test predictions of its supersymetric extensions and search for any new physics. Since its launch, ATLAS has made several important discoveries. In 2012, ATLAS and CMS collaborations announced the discovery of the Higgs boson with a mass of 125.9 ± 0.4 GeV. The entire system of ATLAS is designed using the latest technologies and during development, new detectors and components had to be developed.

The ATLAS consists of many subdetectors which have a specific purpose. The inner subdetector (the inner detector, ID) is designed to measure properties (charge, momentum, trajectory and point of origin) of the charged particles, while calorimetry systems measure their energy. The ATLAS is symmetric in the forward-backward direction with respect to the interaction point. It can be divided into barrel section, end-caps and forward region. The interaction point in the beryllium beam-pipe is surrounded by a barrel region which is enclosed by the endcap region. Outside of barrel in the direction of the beamline at high pseudorapidity is the forward region. This section provides brief overview of main functional parts of the ATLAS detector.

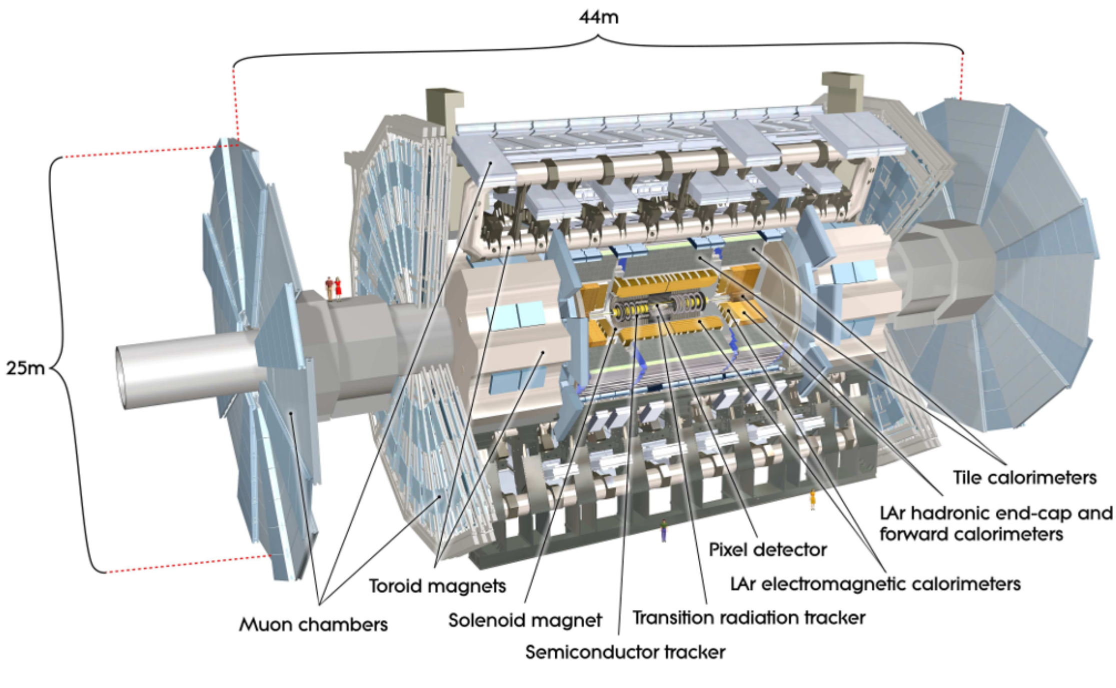

Figure 2.2: ATLAS detector cut-away view with its subdetectors highlighted. [23]

2.2 Tracking

Tne inner detector is designed to provide an excellent momentum resolution for charged particles and both primary and secondary vertex position measurements with high precision in the pseudorapidity range of $|\eta| < 2.5$. It also provides electron identification over the region of $|\eta| < 2.0$.

The ID consists of three independent sub-detectors. All of them are designed to withstand high-radiation environment. The innermost detectors are the silicon pixel detector and silicon microstrip trackers (SCT), which have fine granularity and cover the region up to $|\eta| < 2.5$. Pixel and SCT detectors are supplemented with the straw tubes of the Transition Radiation Tracker (TRT), that provides hits in larger radii. The combination of Pixel, SCT and TRT detectors provides a high precision measurement of position in both coordinates $R - \Phi$ and z.

The inner detector is contained within a cylindrical envelope of a length of ± 3512 mm and of a radius of 1150 mm, and is immersed in a 2 T magnetic field generated by the central superconducting solenoid. As can be seen in figure 2.3, the detectors are arranged as concentric cylinders around the beam axis in the barrel region. In the end-cap regions, there are pixel modules located on disks perpendicular to the beam axis. All detectors are mounted on a support structure, which is made of carbon fibers to ensure good mechanical properties, thermal conduction and low material budget. The support structure is designed to ensure high stiffness and stability, with less than 10 µm displacements under the expected temperature and humidity variations. The dimensions of envelopes of all sub-detectors are listed in [23, p. 8].

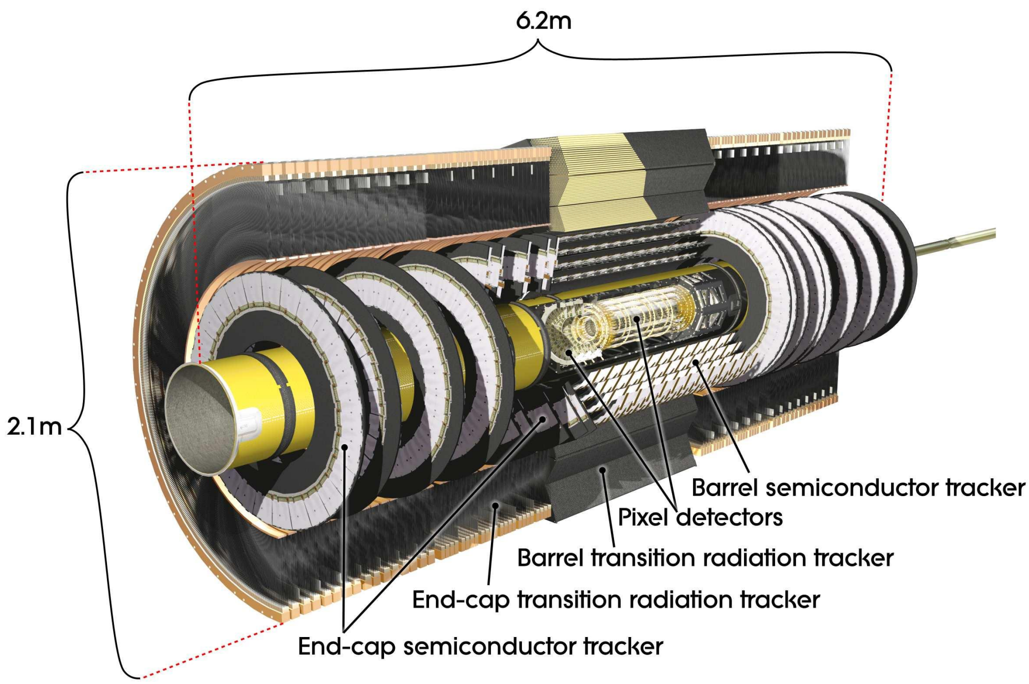

Figure 2.3: ATLAS inner detector cut-away view. [23]

2.2.1 Pixel detector

The pixel detector contains three layers of the pixel modules in the barrel region (called ID layers 0-2) and two end-caps, each with three disk layers. The 0^{th} layer is also referred to as B-layer. The barrel part is divided into 112 staves and an end-cap into 48 sectors. Detailed dimensions of pixel detector are listed in Table 2.1.

The layers are equipped by silicon pixel detectors with nominal pixel size of $50 \times 400\ \mu\text{m}^2$. The sensor thickness is approximately 250 μm. Each pixel sensor is bump-bonded through hole in the sensor passivation layer to front-end readout electronic chip. One sensor is able to provide 46080 readout channels, thus leading to approximately 80.4 million readout channels for the whole pixel detector.

Silicon pixel sensors use planar technology with oxygenated n-type wafers and are read out on the n^+-implanted side of the sensor. The opposite side of the electrodes is in contact with a p^+ layer. This option was chosen despite its higher cost and complexity. One of the advantage of this technology is that highly oxygenated material has been shown to have increased radiation tolerance to a defects produced by a charged hadrons.

To contain reverse annealing and to reduce the leakage current, the sensors are operated in the temperature range of -10 °C to -15 °C . This is provided by aluminium cooling tubes with freon evaporating medium, which are part of bare staves. Heat conduction between cooling tubes and support plates is provided by a thermal compound. Main parameters of the pixel detector are summarized in the Table 2.3.

During first long shutdown between years 2013 and 2015, upgrades are being made. The fourth layer of the pixel detector is added. This layer will be placed between beampipe and current b-layer and is called the Insertable B-layer (IBL). This IBL will be equipped with new sensors using planar n-in-n and 3D double-sided n-in-p technology. These sensors have finer granularity of $50 \times 250\ \mu\text{m}^2$ and besides higher radiation tolerance, new readout chip FE-I4 has lower noise and power consumption. More information about upgrades can be found in [24].

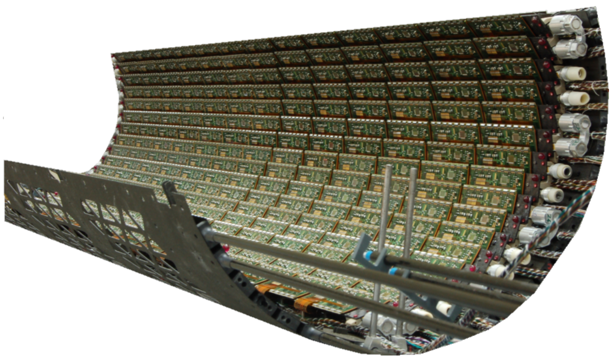

Figure 2.4: Pixel layer equipped by pixel sensors mounted on staves. Each stave contains 13 modules. [25]

2.2.2 SCT detector

SCT detector consist of four layers of double detectors in the barrel region (called ID layers 3-6) and two end-cap regions, each containing nine layers. Layers are equipped by modules which consist of 80 μm pitch micro-strip sensors with thickness 285 ± 15 μm, providing $R - \Phi$ coordinates. For rectangular barrel sensors, two 6 cm long daisy-chained sensors were chosen. Contrary to the rectangular barrel sensors, radial strips with constant azimuth were chosen in the end-cap and they are arranged in a wedge geometry.

Barrel	Radius (mm)	Staves	Modules	Pixels
IBL	25.7	14	224	6.02×10^6
Layer-0	50.5	22	286	13.2×10^6
Layer-1	88.5	38	494	22.8×10^6
Layer-2	122.5	52	676	31.2×10^6
End-cap (one side)	**z (mm)**	**Sectors**	**Modules**	**Pixels**
Disk 1	495	8	48	2.2×10^6
Disk 2	580	8	48	2.2×10^6
Disk 3	650	8	48	2.2×10^6

Table 2.1: The geometry and dimensions of each barrel layer of the pixel detector and end-cap disks with recently added insertable B-layer. [26]

Every two sensor modules are glued together in the barrel region within a hybrid module. On one detector layer, there are 2 sensor layers rotated within their hybrids by ±20 mrad around the geometrical center of the sensor. This allows sensor to measure both $R - \Phi \times z$ coordinates. Sensors are glued on a 380 µm thick thermal pyrolytic graphite (TPG) base-board, which provides mechanical and thermal support structure. Tables 2.2 show SCT barrel detector parameters in detail. In the end-cap region, the sensors have a two set of strips running radially with relative rotation ±20 mrad to provide both $R - \Phi \times z$ coordinates with required resolution.

For reason of cost and reliability, the sensors of SCT use classic single-sided p-in-n technology. The sensors are connected to a binary signal readout chips. The readout hybrid of each SCT module houses 12 identical readout chip, each with 128-channels to read-out with a total of 1536 sensor strips per module. In total, the SCT provides approximately 6.3 million readout channels.

Similar to the pixel detector, SCT must be kept at low temperature from -10 °C to -15 °C to contain reverse annealing and to reduce the leakage current. The heat is extracted by evaporate of C_3F_8 liquid at -25 °C , circulating in a cooling pipes attached to each module.

Barrel	Radius (mm)	Modules
Layer-3	284	384
Layer-4	355	480
Layer-5	427	576
Layer-6	498	672

Table 2.2: The number of modules and radius of each barrel layer. [23]

2.2.3 Transition radiation tracker

Main purpose of TRT is to measure transition radiation of charged particles, in order to distinguish between light electrons and other particles, in the pseudorapidity range of $|\eta| < 2.0$. Typically, the TRT gives 36 hits per track, but it provides only $R - \Phi$ information. The TRT consist of 73 layers of straws in the barrel region and 160 straw planes in end-cap. The intrinsic accuracies are shown in table 2.3.

The basic TRT detector elements are polyamide drift straw tubes with diameter of 4 mm. The straw tube walls, operating as cathodes, were especially developed to have good electrical and mechanical properties with minimal wall thickness. The cathodes are designed to operate at -1530 V to give a gain of 2.5×10^4. The anodes with diameter 31 µm are made of tungsten (99.95%) and they are plated with 0.5–0.7 µm layer of gold. They are directly connected to the front-end electronics. The straw tubes are filled by 70% Xe, 27% CO_2 and 3% O_2 mixture with $5 - 10$ mbar over-pressure. TRT provides approximately 351,000 readout channels in total.

Although the TRT is designed to operate at room temperature, the tubes have to be cooled. At LHC rates, significant heat is generated in the straws by the ionisation current in the gas. The heat dissipated by the straws is transferred to the module shell by conduction through the CO_2 gas envelope. Each module shell is cooled by two cooling tubes. These tubes also serve as return pipes for the C_6F_{14} cooling circuits of the front-end electronics.

Detector component	Intrinsic accuracy (μm)		$\|\eta\|$ coverage	Readout channels	Typical number of hits per charged track
	$R - \Phi$	z			
Pixel	10	115	2.5	80 400 000	3
SCT	17	580	2.5	6 300 000	4
TRT	130	-	2.0	351 000	36

Table 2.3: Main parameters of inner detector system. [23]

2.3 Calorimetry

Calorimetry system is designed to provide good energy resolution for measurement of electromagnetic and hadronic showers, and it must also limit punch-through into the muon system. Calorimetry system consist of two separate calorimeters using different designs suited to the widely varying requirements of the physics processes of interest, and it cover region up to $|\eta| < 4.9$. Over the η region matched to the inner detector, the fine granularity of the EM calorimeter is ideally suited for measurements of electrons and photons. There is coarser granularity in the rest of the detector, but calorimeters are precise enough to satisfy the physics requirements for jet reconstruction and $E_{\mathrm{T}}^{\mathrm{miss}}$ measurements.

The calorimetry system layout can be seen in figure 2.5. More information about η coverage of each subdetector, number of layers and their granularity can be found in [23, p.10].

2.3.1 Electromagnetic calorimeter

The EM calorimeter is divided into a barrel and two end-caps (EMEC). The EM calorimeter is a lead-liquid argon (LAr) detector with accordion-shaped kapton electrodes and lead absorber plates. The EM calorimeter has complete Φ symmetry without azimuthal cracks.

In region of $|\eta| < 1.8$, a presampler detector layer is placed in front of the inner surface. The presampler detector is manufactured using LAr technology. This provides electron and photon energy loss corrections. Over the region of $|\eta| < 2.5$, the EM calorimeter is segmented in three sections in radius. For the rest, the calorimeter is segmented in two sections in radius and has a coarser granularity.

The readout electrodes are located in the gaps between the absorbers and consist of three conductive copper layers separated by insulating polyamide sheets. The first layer of each calorimeter is read out from the front, whereas the second and third layers are read out from the back. The first layer is finely segmented along η. The second layer collects the largest fraction of the energy of the electromagnetic shower. The third layer collects only the tail of the electromagnetic shower and is therefore less segmented in η.

2.3.2 Hadronic calorimeters

The hadronic calorimeter is placed directly outside the EM calorimeter envelope. Similarly to the electromagnetic calorimeter, it is divided into barrel and 2 endcaps, but it also has extended barrel and forward

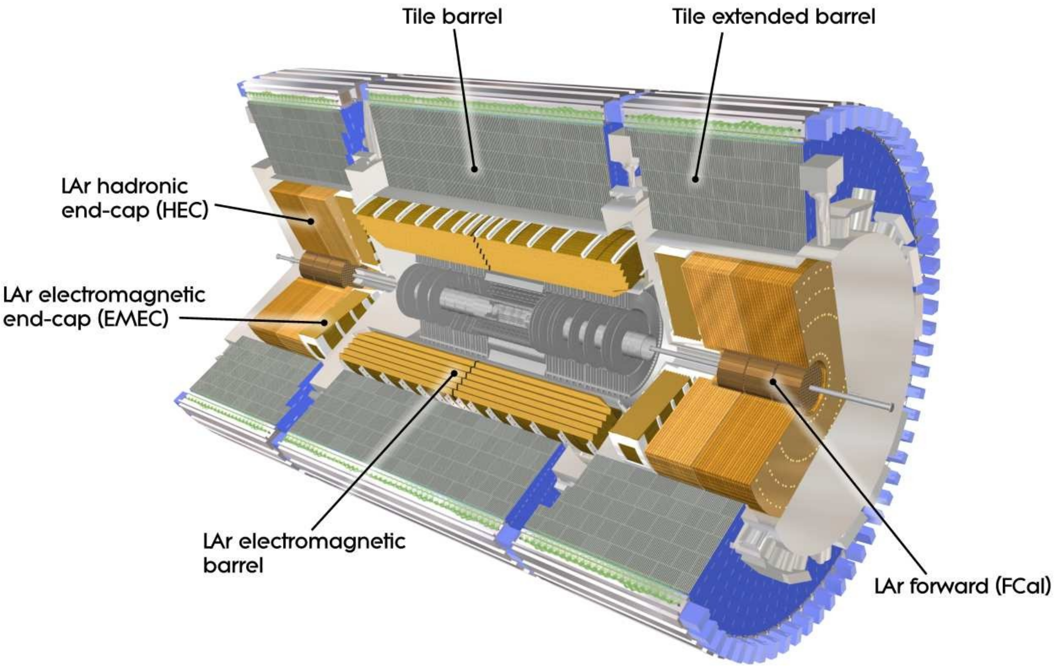

Figure 2.5: ATLAS calorimetry system cut-away view. [23]

detectors. The two different calorimeter types are used to detect hadronic showers.

Scintillator tile calorimeter is placed in barrel and extended barrel region. It is a sampling calorimeter using steel as the absorber and scintillating tiles as the active material. Tile barrel covers the region of $|\eta| < 1.0$ and it is segmented in radius into three layers. Tile extended barrel covers region $0.8 < |\eta| < 1.7$ and is also segmented into three layers. Scintillating tiles are read out by wavelength shifting fibers into multi-channel photomultiplier tubes.

LAr hadronic calorimeters are placed in end-cap region. Hadronic end-cap Calorimeter (HEC) is a copper/liquid-argon sampling calorimeter with a flat-plate design. The HEC covers range $1.5 < |\eta| < 3.2$ and consists of two wheels in each end-cap. Important fact is, that the HEC is able to detect muons and it allows the measurement of the radiative energy loss.

The hadronic calorimetry is extended to larger pseudorapidities by the forward calorimeters (FCal). They cover region of $3.1 < |\eta| < 4.9$. The FCal uses copper-tungsten/liquid-argon detectors and share the same cryostat with EMEC and HEC calorimeters to reduce radiation background levels in the muon spectrometer. Each FCal is split into one electromagnetic module made of copper and two hadronic modules made of tungsten. A more detailed description of FCal and the other calorimeters can be found in [23].

2.4 Muon system

The muon system is designed to detect charged particles exiting the barrel and end-cap calorimeters, and to measure muon momentum in the pseudorapidity range of $|\eta| < 2.7$. It measures properties of muon tracks bent by the large superconducting air-core toroid magnets. Detectors are situated in the barrel, end-cap and also in the transition regions ($1.4 < |\eta| < 1.6$), where the tracks are bent by combination of barrel toroid and end-cap magnets. In the barrel region, tracks are measured in chambers arranged in three cylindrical layers around the beam axis, while in the transition and end-cap regions, the chambers are installed in planes perpendicular to the beam axis, also in three layers. Over most of the η-range, a precision measurement of the track coordinates is provided by the Monitored Drift Tubes (MDT). At large pseudorapidities, the Cathode Strip Chambers (CSC) with higher granularity are used to withstand demanding rate and background conditions.

The pseudorapidity range of $|\eta| < 2.4$ is covered by an additional trigger system which is equipped with Resistive Plate Chambers (RPC) in the barrel ($|\eta| < 1.05$) and Thin Gap Chambers (TGC) in end-cap ($1.05 < |\eta| < 2.4$) regions, respectively. The main purpose is to provide fast track information for triggering purposes with well-defined p_T thresholds.

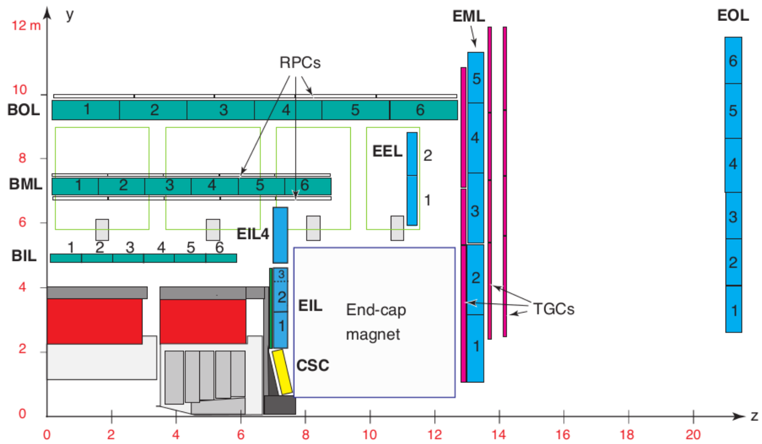

Figure 2.6: Cross-section of the quadrant of the muon system in a plane containing the beam axis. [27]

2.4.1 Monitored drift tube chambers

The Monitored Drift Tube chambers (MDT), used to provide momentum measurement and determine coordinate of the track in the bending plane, combine high measurement accuracy, predictability of mechanical deformations and simplicity of construction. MDT's cover region $|\eta| < 2.7$ and are arranged in three layers.

The chambers consist of 2 superlayers each with 3 or 4 layers of tubes and support frame. This support frame has rectangular shape in the barrel and trapezoidal shape in the end-cap. The frames also carry most of the interfaces to gas supplies, and to the electrical, monitoring and alignment services. MDT provide a high level of operational reliability, because the failure of a single tube does not affect the operation of most of the others. The average spatial resolution obtained from tests is about of 80 μ m.

With a total number of 1150 chambers, MDT system provides approximately 354000 readout channels.

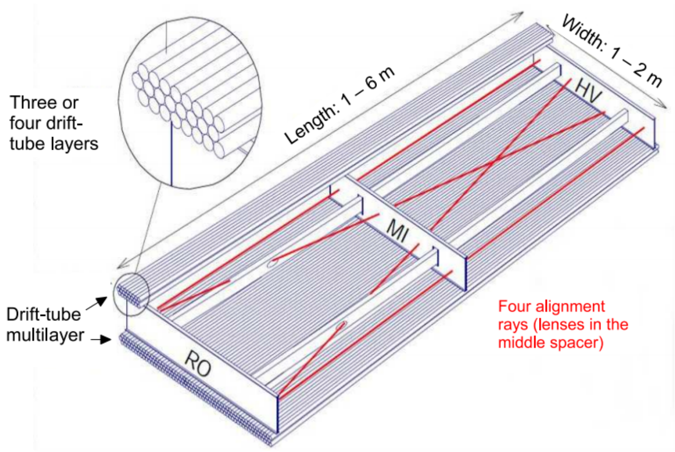

Figure 2.7: MDT chamber structure. [23]

2.4.2 Cathode-strip chambers

The MDT's are not efficient at high counting rates. That is why MDT's are replaced by CSC's at first layer in the forward region for rapidities in range of $2 < |\eta| < 2.7$.

The CSC's are multiwire proportional chambers with cathode planes segmented into strips. The position of track is obtained by interpolation between the charge induced in neighbour strips. The charge interpolation is a relative measurement and the resolution is determined only by the signal-to-noise ratio. The spatial resolution of CSC is about 60 µm in bending plane.

2.4.3 Resistive Plate Chambers

The trigger system in barrel consists of RPCs which are arranged in three layers like the MDT chambers. Outer layer of RPC's is able to select high momentum tracks with threshold in range from 9 to 35 GeV (high-p_T trigger). Two inner RPC's layer provide low momentum trigger with thresholds from 6 to 9 GeV. Each RPC consist of two independent layers for η and Φ measurement.

The RPC is a fast gaseous parallel electrode-plate detector. RPCs consist of two parallel plates made of a high resistivity plastic material separated by a gas volume. A charged particle crossing gas volume create an avalanche of electrons drifting toward the anode. The detection efficiency of single layer is greater than 97% [23].

2.4.4 Thin Gap Chambers

For the endcap trigger system, the TGCs were chosen. They are arranged in four planes around the beam axis. In addition, the TGC's are used to determine second azimuthal coordinate of the muon track. The layers used for position measurement are not used for triggering.

Physically, the TGCs are multiwire proportional chambers with cathode distance smaller than wire-to-wire distance. Position measurements are obtained from both the pick-up strips and the wires. The small wire-to-wire distance lead to very good time resolution. Thus, Signals arrive with 99% probability inside a time window of 25 ns [28].

Chapter 3

Properties of quarkonia

3.1 Heavy Quarkonia

The quarkonia are a bound state of $\mathcal{Q}\bar{\mathcal{Q}}$ pair made of quarks with the same flavour. The combined pair is flavourless and its energy-level structure is reminiscent of positronium. A designation heavy quarkonia is usually attributed to Charmonium ($c\bar{c}$) and Bottomonium ($b\bar{b}$). The top quark does not occur in hadrons due to its large mass and short lifetime, it decays before it has chance to hadronize.

Because quarkonia are almost nonrelativistic, they also have spectrum similar to the hydrogen atom. However, unlike its analogs governed mainly by the electrostatic Coulomb force, the properties of charmonium are determined also by the strong interaction, so that the quarkonia system was, the simplest object for a study of the strong interactions. Thus, the studies of charmonium spectrum and its other properties is important, because it tests various theoretical models and predictions which struggle to describe strong interaction in the low energy region.

3.2 J/ψ discovery

The existence of the c quark was predicted by S. Glashow, J.Liopoulos and L. Maiani in 1970 as mentioned in chapter 1.2.2. Two separate groups led by Samuel C.C. Ting [29] and Burton Richter [30] participated in the discovery of J/ψ and therefore a c quark. They observed a vector meson with higher mass than then known ω, ρ and ϕ vector mesons consisting of lighter quarks. The first group named the new meson J while the second ψ. Both groups announced their discoveries on 11$^{\text{th}}$ November 1974. Thus, the new particle was named J/ψ. Following paragraph provides further details about experiments leading to the discovery of J/ψ.

3.2.1 Samuel C.C. Ting and BNL experiment

Samuel C.C. Ting was leading a group from MIT and Brookhaven National Laboratory (BNL) performing measurements of the rates of e^+e^- pairs in collisions of protons with a beryllium target. To detect e^+e^- pairs, they build pair spectrometer, able to measure quite accurately the invariant mass of the pair. Both of these experiments investigated the Drell-Yan process, whose motivation lay in the quark–parton model.

The important step in measurement of e^+e^- pairs was to separate electrons from hadrons. For this reason, the Čerenkov counters were used. The Čerenkov-counter approach is very effective in rejecting hadrons, but can be implemented easily only over a small solid angle. That is why Ting's experiment used two magnetic spectrometers to measure separately the e^+ and e^-. The beryllium target was selected to minimize multiple Coulomb scattering.

In October 1974, C.C. Ting's group was taking collision data with their pair spectrometer and observed a narrow resonance at 3.1 GeV in the invariant mass spectrum of e^+e^-. Ting's group named new observed particle as J.

3.2.2 Burton Richter and SPEAR

The Burton Richter lead a research group at Standford laboratory and they had an ambition to construct an e^+e^- collider ring called SPEAR. The ring was filled by the Standford Linear Accelerator (SLAC). Burton's group studied e^+e^- collisions in the 2.5 to 7.5 GeV center-of-mass energy region.

In order to detect outgoing particles, they built a multipurpose large-solid-angle magnetic detector, the SLAC-LBL Mark I. In the middle of the detector, there was a cylindrical magnetoselective spark chamber inside a soleonidal magnet of 4.6 kG field. This was surrounded by time-of-flight counters and proportional counters.

The Burton's group was measuring annihilation cross section into hadrons with energy steps of 200 MeV. Because the energy steps were too large with respect to the width of J/ψ resonance, they did not observe any significant change of cross-section, only a small irregularities at the center-of-mass energy 3.2 GeV. That is why they decided to check this region by taking additional data at 3.1 and 3.3 GeV. Scanning this region in a very small energy steps revealed an enormous, narrow resonance. The new particle was named ψ. In addition, Burton's group discovered excited state of this new particle, called ψ' ($\psi(2S)$ in spectroscopic notation), and started intense spectroscopic work on this resonance.

3.3 The Spectrum of Charmonium States

To characterize quarkonium states, the J^{PC} formalism is often used, where J is total angular momentum, P is parity and C is charge conjugation of a particular state. This description holds information about corresponding quantum numbers. Because quarkonium is bound state of two quarks, its structure and energy levels can be described by the following scheme 3.1.

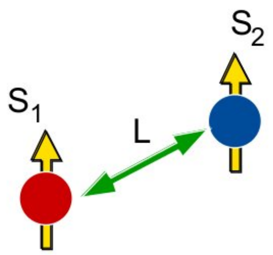

$$S = S_1 + S_2$$
$$J = L + S$$
$$P = (-1)^{L+1}$$
$$C = (-1)^{L+S}$$

Figure 3.1: Di-quark interaction, where S_1, S_2 are spins angular momenta of the constituent quarks, L is orbital angular momentum, and P and C are eigenvalues of parity and charge conjugation operator, respectively. [31]

This description gives the constraints on values of J, P and C. The states, which meet this conditions, are denoted as allowed states. But there exist several states, which do not meet this constraints. This states are denoted as exotic states. The total spin S takes the values 0 or 1, thus splitting the four possible spin states of the pair into a singlet and a triplet. Furthermore, the excitation of the radial motion of the $c\bar{c}$ pair results in a spectrum of levels with the same L, S and J, differing by the "radial" quantum excitation number n_r. In addition, each state of charmonium can be described by a symbol

$(n_r+1)^{2S+1}L_J$. The values of L , $L = 0, 1, 2, \ldots$ are written as $S, P, D, \ldots$ with respect to the historical atomic physics notation.

In figure 3.2, the well known state of charmonium family with $n_r = 0$ called J/ψ can be seen as well as its first excited state $\psi(2S)$. The J/ψ is a vector meson with mass $m_{J/\psi} = (3096.916 \pm 0.011)$ MeV. Thus, they have three degrees of freedom in polarization, two transverse and one longitudinal.

In figure 3.2, the χ_c triplet can be seen also. The states under $D\bar{D}$ threshold decay via di-lepton channel with high probability and it is simple to detect them, but if binding energy exceeds energy of $u\bar{u}$ quark pair, then very probably it will decay by strong interaction into D and $\bar{D}$ mesons, which in turn decay. The $D\bar{D}$ threshold is not the only one threshold in the system. The quarkonium state can decay via multiple channels with increasing binding energy. The diagram of charmonium states with thresholds is shown in figure 3.2.

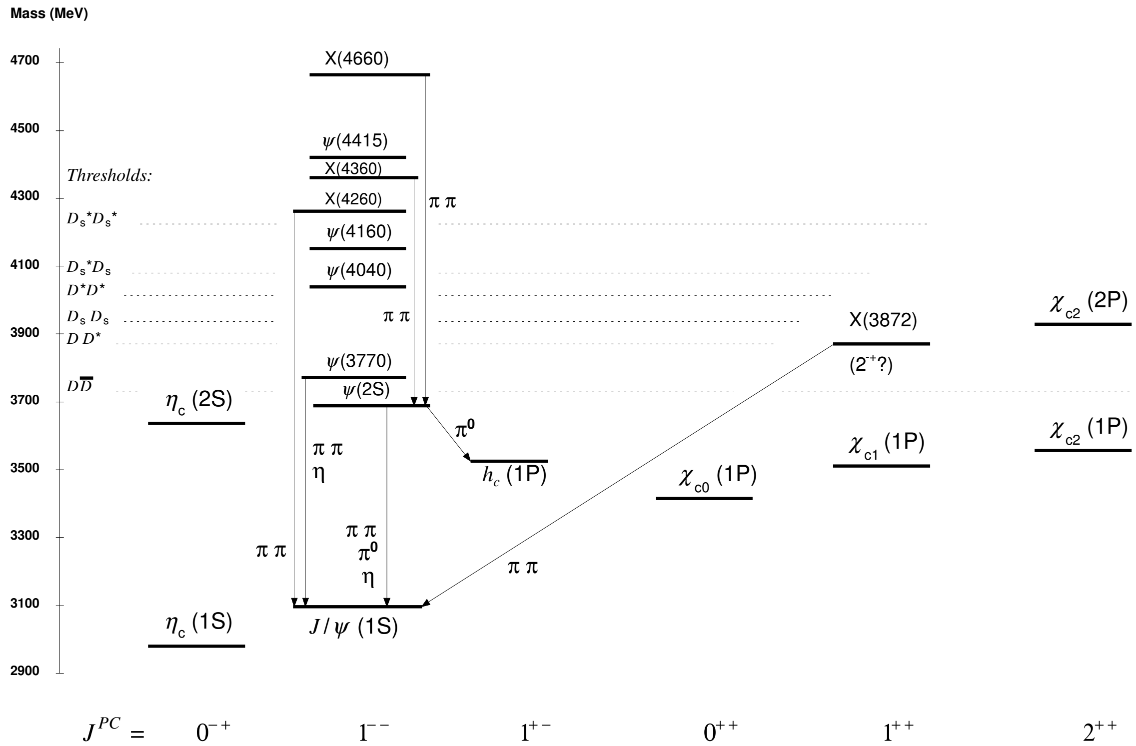

Figure 3.2: The energy levels with thresholds and several hadronic decay channels of charmonium states. [4] The J^{PC} notation is explained in section 3.3.

3.4 Present status of quarkonium spectroscopy

At present, the studies of quarkonium spectra are underway at several experiments i.e. CLEO, Belle, ATLAS, CMS and LHCb. The groups at this experiments are trying to observe states predicted by the theory and on the other hand explain observed states which do not fit into any model. The groups also focus on the measurement of quantum numbers, masses, and widths of heavy quarkonium (or quarkonium-like) bound states.

During the last decade, at least nine conventional heavy quarkonium states were observed, and also nineteen unconventional heavy quarkonium states. Now the work is progressing on a clarification of their properties and studying their decays and transitions. The production mechanisms of quarkonium are intensively studied. More information is listed in [32].

State	**Mass [MeV]**	**Width [MeV]**	J^{PC}	$(n_r+1)^{2S+1}L_J$
$J/\psi(1S)$	3096.916 ± 0.011	0.0929 ± 0.0028	1^{--}	1^3S_1
$\psi(2S)$	$3686.109^{+0.012}_{-0.014}$	0.286 ± 0.016	1^{--}	2^3S_1
$\eta_c(1S)$	2980.3 ± 1.2	32.2 ± 1.0	0^{-+}	1^1S_0
$\eta_c(2S)$	3639.4 ± 1.3	$11.3^{+3.2}_{-2.9}$	0^{-+}	2^1S_0
$h_c(1P)$	3525.67 ± 0.32	$0.70 \pm 0.28 \pm 0.22$	1^{+-}	1^1P_1
$\chi_{c0}(1P)$	3414.75 ± 0.31	10.5 ± 0.8	0^{++}	1^3P_0
$\chi_{c1}(1P)$	3510.66 ± 0.07	0.88 ± 0.05	1^{++}	1^3P_1
$\chi_{c2}(1P)$	$3556.20.2 \pm 0.09$	1.95 ± 0.13	2^{++}	1^3P_2
$\psi(3770)$	3778.1 ± 1.2	27.5 ± 0.9	1^{--}	1^3D_1
$X(3872)$	3871.68 ± 0.17	< 1.2	1^{++}	–
$\chi_{c2}(2P)$	3927.2 ± 2.6	24 ± 6	2^{++}	2^3P_2
$\psi(4040)$	4039.6 ± 4.3	84.5 ± 12.3	1^{--}	–
$\psi(4160)$	4191.7 ± 6.5	71.8 ± 12.3	1^{--}	–
$X(4260)$	4250 ± 9	108 ± 12	1^{--}	–
$X(4360)$	$4361 \pm 9 \pm 9$	$74 \pm 15 \pm 10$	1^{--}	–
$\psi(4415)$	4415.1 ± 7.9	71.5 ± 19.0	1^{--}	–
$X(4660)$	$4664 \pm 11 \pm 5$	$48 \pm 15 \pm 3$	1^{--}	–

Table 3.1: The table of conventional charmonium states under $D\bar{D}$ threshold and possible candidates to be a higher excited states of charmonium. The values are taken from PDG [4]. The J^{PC} notation is explained in section 3.3. The states under $D\bar{D}$ threshold fits on $((n_r+1)^{2S+1}L_J)$ spectroscopic description. The states above the $D\bar{D}$ are possible candidates to be the higher excited states of charmonium, but the other explanation are tetraquarks.

Chapter 4

Experimental data analysis

In this chapter, the basics of data analysis tools used in this analysis and data acquisition and processing are described. Further, the analysis procedure and results are presented.

4.1 Coordinate system

The coordinate system describing the detector phase space is usually set up with the z-axis parallel to the beam direction and the x-y plane transverse to the beam direction. The variables measured in the transverse plane are denoted with a T subscript. The positive x-axis is defined as pointing from the interaction point to the center of the LHC ring, the positive y-axis is defined as pointing upwards. The positive direction of z-axis is defined so as to create the right-handed coordinate system.

For the track measurement, it is easier to determine the azimuthal angle Φ, which is measured around the beam axis, and the polar angle Θ, which is an angle between the beam axis and the measured point. Using this phase space description, the following terms are introduced.

The pseudorapidity is defined as

$$\eta = -\ln \tan \frac{\Theta}{2}. \tag{4.1}$$

In the case of massless nonrelativistic objects, the pseudorapidity is equal to the rapidity

$$y = \frac{1}{2} ln \frac{E + p_z}{E - p_z}. \tag{4.2}$$

The distance ΔR in the pseudorapidity-azimuthal angle space is defined as

$$\Delta R = \sqrt{\Delta\eta^2 + \Delta\Phi^2}. \tag{4.3}$$

4.2 ROOT Framework

The ROOT framework [33] is an object oriented analysis tool for data processing developed at CERN and is available under the LGPL license. ROOT is written in C++ and provides an advanced statistical analysis and visualization tools. The command language as well as the scripting language is C++. The ROOT framework provides containment for analysis processing and storage of analysis results in the proprietary ROOT tree structure. It also allows usage of parallel computing tools for effective processing of large data files. The analysis presented here is processed on the ROOT version 5.32.04 using the CINT interpreter.

4.3 Data acquisition and processing

The proton-proton collision data, at a center-of-mass energy of 8 TeV, are the basis of this analysis. The data were taken during periods G and E of the ATLAS 2012 run and only the data collected with a stable beam operation are used. The criteria of quality were applied at the luminosity block levels, where the luminosity block, which lasts 60 seconds, is an atomic unit of the ATLAS data. The detector settings such as prescale factors are unchanged during a luminosity block. To ensure that only the data passing all quality tests are used, the data are filtered by a Good Runs List (GRL).

The integrated luminosity recorded during the ATLAS ready[1] after accounting for the L1 veto reach in periods G and E value of 3.08233 fb^{-1} with a relative statistical uncertainty of 3.6% [34]. Figure 4.1 shows evolution of the integrated luminosity during stable beams and for pp collisions at 8 TeV center-of-mass energy in 2012.

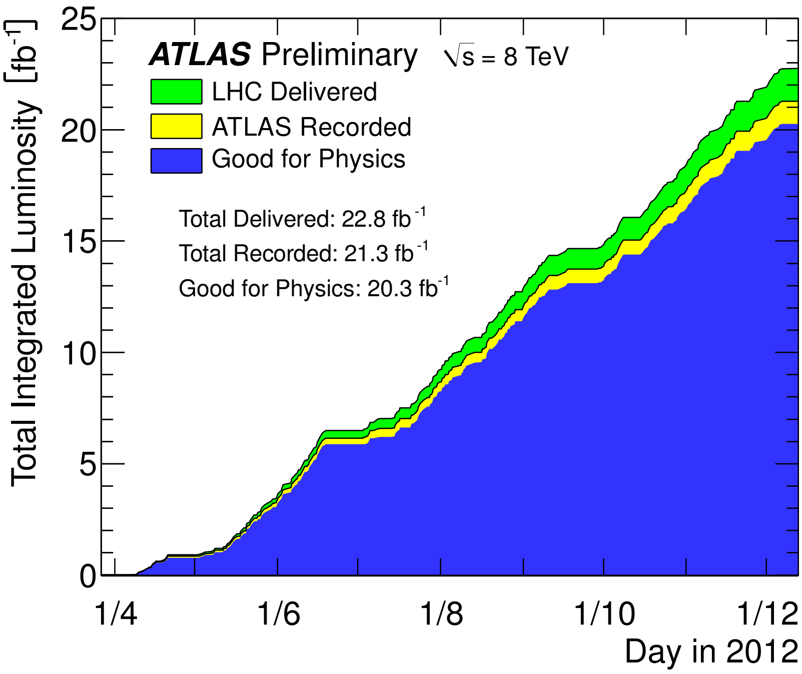

Figure 4.1: Cumulative luminosity versus time delivered to (green), recorded by ATLAS (yellow), and certified to be good quality data (blue) during stable beams and for pp collisions at 8 TeV center-of-mass energy in 2012. The delivered luminosity accounts for the luminosity delivered from the start of stable beams until the LHC requests ATLAS to put the detector in a safe standby mode to allow a beam dump or beam studies. The recorded luminosity reflects the DAQ inefficiency, as well as the inefficiency of the so-called "warm start": when the stable beam flag is raised, the tracking detectors undergo a ramp of the high-voltage and, for the pixel system, turning on the preamplifiers. The data quality assessment shown corresponds to the All Good efficiency shown in the 2012 DQ table. The luminosity shown represents the preliminary 8 TeV luminosity calibration. Data quality has been assessed after reprocessing. [35]

[1] ATLAS ready is a flag assigned to data, when the beam was stable and all detectors were running.

For the purpose of this analysis, the $J/\psi \rightarrow \mu^+\mu^-$ decay channel was chosen, because the muons have clean detector signature. In this section, the path of signal observed after muons passing through the ATLAS detector is described in more detail.

4.3.1 Triggers

The trigger system is used to evaluate which collision events should be saved to disk for further analysis. The ATLAS detector uses a three-level trigger system. The first stage of the triggering process is implemented in the L1 trigger. For the measurements presented here, the muon trigger L1_2MU4 is used. This trigger is based on the muon reconstruction in the RPCs for the barrel and the TGCs for the end-cap region. The L1_2MU4 trigger requires two muons with p_T larger than 4 GeV. In addition, the L1 trigger carries the rough detector position (φ, θ) information to be investigated by the next trigger levels.

If an event passes through the L1 trigger, a candidate event is sent to the software based High Level Trigger (HLT), which is subdivided to the Level 2 (L2) trigger and the Event Filter (EF). The HLT reconstructs tracks, higher-level physical objects, and matches the detector region reported by the L1 trigger. The L2 trigger employs fast reconstruction algorithms which operate on a segment of the detector in the region provided by the L1 trigger, and after this step, if triggering conditions are satisfied, the EF makes an online reconstruction of the whole event using the full detector information. The data triggered by the L1_2MU4 and confirmed at the high level trigger are denoted EF_2mu4.

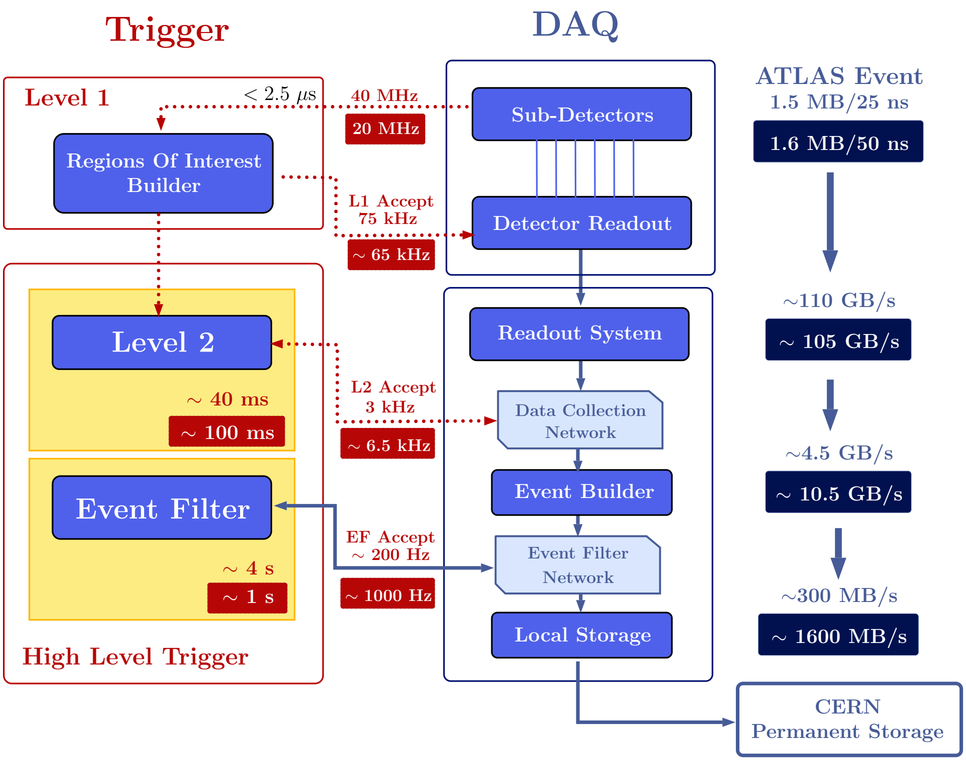

Figure 4.2: The ATLAS trigger data acquisition diagram. The design parameters are reported for each component. The highlighted numbers refer to the 2012 peak values of decision time, rate and bandwidth. [36]

The offline reconstructed events are divided into data streams according to the triggers they fire. For a given trigger sample, the offline muon pair must pass the same p_T cuts as are applied in the trigger. They must also have an absolute pseudorapidity < 2.3. The invariant mass window in the region of the J/ψ mass window ($2.5-4.3$ GeV) calculated using the trigger objects is denoted with a suffix _Jpsimumu.

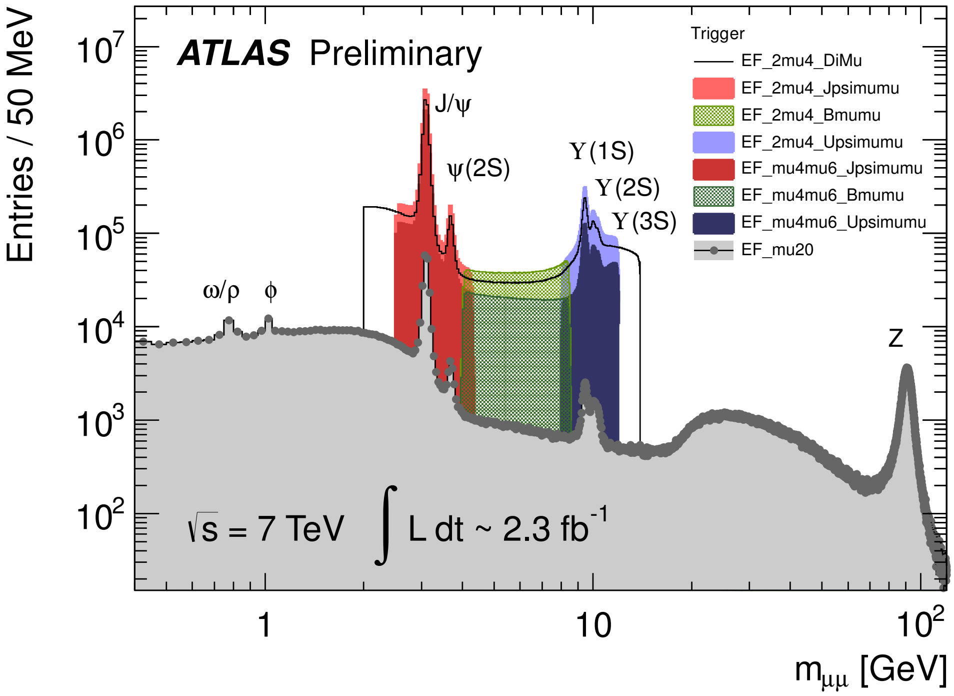

Figure 4.3: Invariant mass of oppositely charged muon candidate pairs selected by a variety of triggers. [37]

4.3.2 Event reconstruction

The raw data input was reconstructed by the ATLAS offline software framework Athena. The output of the reconstruction are the Analysis Object Data (AOD) files. [38] The AOD contain a summary of the reconstructed event, including all physics objects in the event. This analysis uses collections of variables suitable for B-physics extracted from AODs known as D3PDs, in particular Onia muons ntuples made from DAOD_JPSIMUMU containers. The DAOD_JPSIMUMU contains for example a data container of J/ψ candidates called JpsiCandidates and all reconstructed muons which are in the event.

Muon reconstruction

To reconstruct muon tracks, several different strategies have been developed using physics signatures in the inner detector, calorimeters and muon detector system. Muons can be classified into four categories according to the signatures left in the detector:

- *Standalone* muons are identified using only Muon Spectrometer. The tracks are extrapolated to the beam region to give the track parameters. Due to the position and momentum resolution of the muon chambers, their parameters are not measured as precisely as in other muon reconstruction types, but provide muons from higher rapidity $|y| < 2.7$.

- *Combined* muons are formed by matching the Inner Detector track to the Muon Spectrometer track. Two algorithms, Staco and Muid, are used to identify the combined muons. They have the most precisely measured parameters.

- *Tagged* muons are the ID tracks matched to the hits in the muon segments in the Muon Spectrometer. There are two tagging algorithms, MuTag and MuGirl, propagating all inner detector tracks with a sufficient momentum out to the first station of the muon spectrometer and search for nearby segments.

- *Calorimeter tagged* muons use information about energy deposit in the calorimetry system matched to the ID tracks. The calorimeter muons have lower purity and efficiency than the muons reconstructed in the muon system.

To reconstruct the J/ψ candidates, only combined muons are used to guarantee the purity of the signal. [39]

Di-muon candidates reconstruction

To reconstruct the combined di-muon candidates, two algorithms called the STACO (Statistical combination of the inner and outer track vectors) and Muid (a partial refit using the original hits in both ID and MS) are used. Each of these algorithm produces its own chain called STACO and Muid. Because both of these chains demonstrated their excellent capabilities of supporting physics analyses with muons, they have been merged into a third, unified chain called Muons.

4.3.3 Event selection

In the analysis presented here, the di-muon pairs have to meet the following conditions:

- pass EF_2mu4_JPsimumu trigger in the region of $|\eta| < 2.3$ and invariant mass window of 2.5 - 4.3 GeV,

- the offline reconstructed muons must have $p_T > 4$ GeV,

- the muons in a pair must have opposite charges,

- the EF trigger muon candidates must be matched to within $\Delta R < 0.01$ of the offline muon tracks.

The last constraint rejects about 5% of the J/ψ candidates on the EF level and ensures, that the trigger was fired by a measured muon and so the trigger unfolding can be performed.

4.3.4 Monte Carlo data

The Monte Carlo (MC) data produced by the ATLAS B-physics group are compared to the measurements. The MC datasets were produced using the Pythia8B_i generator. The Pythia8B_i generator is a classical Pythia8 adjusted for the needs of B-physics group. [40]

The passage of the generated particles through the detector is simulated with Geant4 [41] and the data are fully reconstructed with the same algorithms that are used to process the data from the detector. The ATLAS Geant4 simulation contains over the million volumes including the active and inactive material to describe the ATLAS geometry.

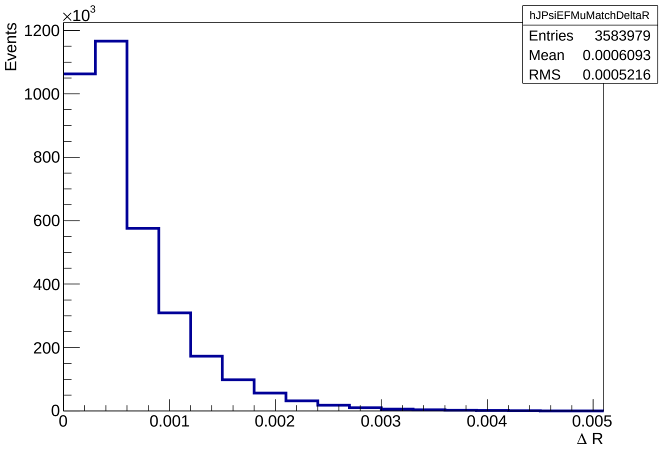

Figure 4.4: EF trigger matching of muons which are matched with offline muon tracks. The ΔR is a distance of the offline reconstructed muons to the muon trigger objects.

4.3.5 Datasets

Table 4.1 summarizes the datasets used in this analysis. The official Monte Carlo data were produced in the early 2012, and these datasets are available on the Grid network. The datasets denoted with _pp are the MC samples which simulate the prompt production of J/ψ, while the datasets denoted with _bb are the MC samples which simulate the non-prompt production of J/ψ to the decay of B mesons.

Dataset Name	Number of events
Data 2012	
data12_8TeV.periodE.physics_Bphysics.PhysCont.DAOD_JPSIMUMU	23422976
data12_8TeV.periodG.physics_Bphysics.PhysCont.DAOD_JPSIMUMU	11919246
MC 2012	
Pythia8B_AU2_CTEQ6L1_pp_Jpsimu4mu4	10 M
Pythia8B_AU2_CTEQ6L1_bb_Jpsimu4mu4	10 M

Table 4.1: The ATLAS datasets used in the analysis.

4.4 Inclusive fiducial $J/\psi \to \mu^+\mu^-$ differential production cross-section

The measurement of the inclusive differential cross-section is made in twelve bins of transverse momentum and two bins of rapidity. The measurement is restricted to the sensitive area of the ATLAS detector. The cross-section in each particular bin is determined as

$$\frac{d^2\sigma(J/\psi)}{dp_T dy} Br(J/\psi \to \mu^+\mu^-) = \frac{N_{corr}^{J/\psi}}{\mathcal{L} \cdot \Delta p_T \Delta y}, \tag{4.4}$$

where Δp_T and Δy are the p_T and y bin widths, $\mathcal{L}$ is the integrated luminosity of the data sample and $N_{corr}^{J/\psi}$ is the number of J/ψ signals for each $p_T - y$ bin after background subtraction and detector efficiency corrections. To determine a true number of J/ψ decays, $N_{corr}^{J/\psi}$, each recorded event is weighted by a weight w. The weight w is defined as

$$w^{-1} = \mathcal{E}_{\text{reco}} \cdot \mathcal{E}_{\text{trig}} \frac{1}{p}, \tag{4.5}$$

where $\mathcal{E}_{\text{reco}}$ is the muon offline reconstruction efficiency, $\mathcal{E}_{\text{trig}}$ is the trigger efficiency and p is the trigger prescale factor.

4.4.1 Reconstruction and trigger efficiency

The reconstruction efficiency $\mathcal{E}_{\text{reco}}$ for a given J/ψ candidate is calculated from single muon reconstruction efficiencies of J/ψ candidate daughter muons $\mathcal{E}_{\mu}^{\pm}(p_T^{\pm}, \eta^{\pm})$ as follows:

$$\mathcal{E}_{\text{reco}} = \mathcal{E}_{\mu}^{+}(p_T^{+}, \eta^{+}) \cdot \mathcal{E}_{\mu}^{-}(p_T^{-}, \eta^{-}). \tag{4.6}$$

The offline single muon reconstruction efficiencies are obtained from the MC data using a tag-and-probe method, where muons are paired with ID tracks ("probes") of the opposite charge. The probes are divided into bins in $p_T(\mu)$ and $q \times \eta(\mu)$. For each bin, a number of matched (for which the probe is reconstructed as a muon) and unmatched (for which the probe is not reconstructed as a muon) J/ψ candidates is calculated. The number of matched and unmatched J/ψ candidates is computed from the invariant mass distribution as a clear signal after background subtraction. The muon reconstruction efficiency for each bin is obtained as a ratio of the matched and total number of candidates.

Similar to reconstruction efficiency, the trigger efficiency $\mathcal{E}_{\text{trig}}$ for given J/ψ candidate is calculated from single muon trigger efficiencies $\mathcal{E}_{\text{RoI}}^{\pm}(p_T^{\pm}, q, \eta^{\pm})$. The trigger efficiency with dimuon correction $c_{\mu\mu}(\Delta R, |y^{\mu\mu}|)$ is equal to

$$\mathcal{E}_{\text{trig}} = \mathcal{E}_{\text{RoI}}^{+}(p_T^{+}, q, \eta^{+}) \cdot \mathcal{E}_{\text{RoI}}^{-}(p_T^{-}, q, \eta^{-}) \cdot c_{\mu\mu}(\Delta R, |y^{\mu\mu}|). \tag{4.7}$$

The single muon efficiency and correction factor is evaluated by the tag-and-probe method. For each $p_T(\mu)$ vs $q \times \eta(\mu)$ bin, the tag is an OR statement of multiple high p_T single EF muon triggers and the probe is EF_2mu4T_Jpsimumu_L2StarB, where each probe event is corrected by the $\mathrm{c}_{\mu\mu}(\Delta R, |y^{\mu\mu}|)$ factor. Each event is also weighted by the average prescale correction factor.

The resulting efficiency maps are shown in figure 4.5 for single muon trigger and figure 4.6 for the muon reconstruction. The efficiencies were provided by the ATLAS B-physics group and are preliminary.

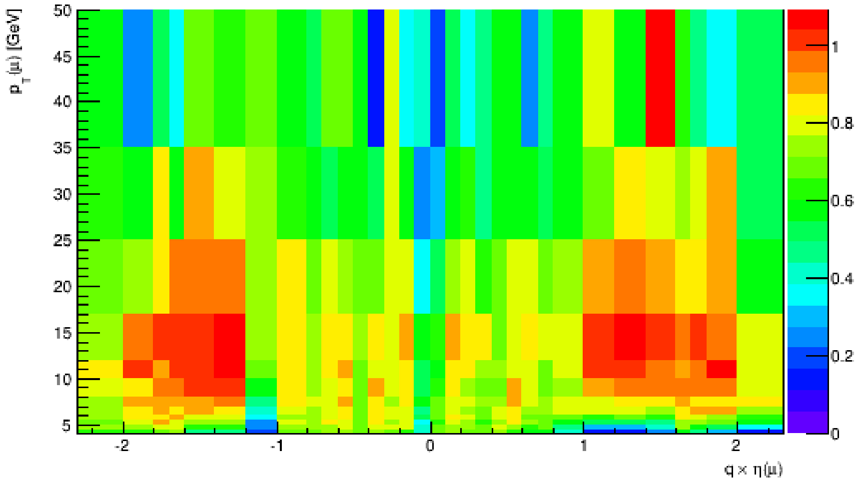

Figure 4.5: The single muon trigger RoI efficiency, $\mathcal{E}_{\mathrm{RoI}}$, as a function of the muon charge-signed pseudorapidity and muon p_T.

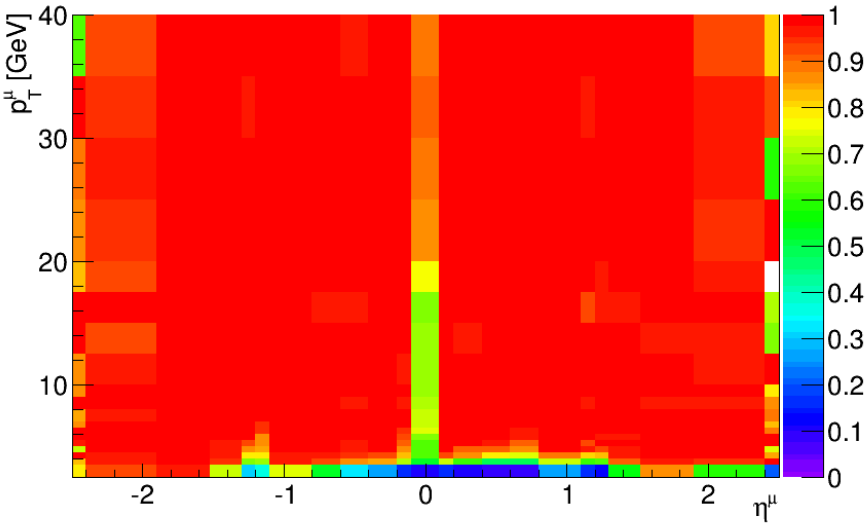

Figure 4.6: The muon reconstruction efficiency map determined from the 2012 data as a function of the muon charge-signed pseudorapidity and muon p_T.

4.4.2 Fit of J/ψ candidates mass distributions

The distribution of J/ψ candidates in $p_T - y$ plane can be seen in figure 4.7. The invariant mass of candidates is restricted to a 400 MeV invariant mass window around the J/ψ PDG mass. In the invariant mass fit, this cut is not used.

The inclusive J/ψ production cross-section is determined in four slices of J/ψ rapidity: $|y| < 0.75$, $0.75 < |y| < 1.5$, $1.5 < |y| < 2$ and $2 < |y| < 2.3$. The selection of rapidity bins was made with respect to the previous ATLAS analysis at 7 TeV [42]. The inclusive J/ψ production cross-section is also determined in eleven slices of J/ψ p_T starting at 7 GeV.

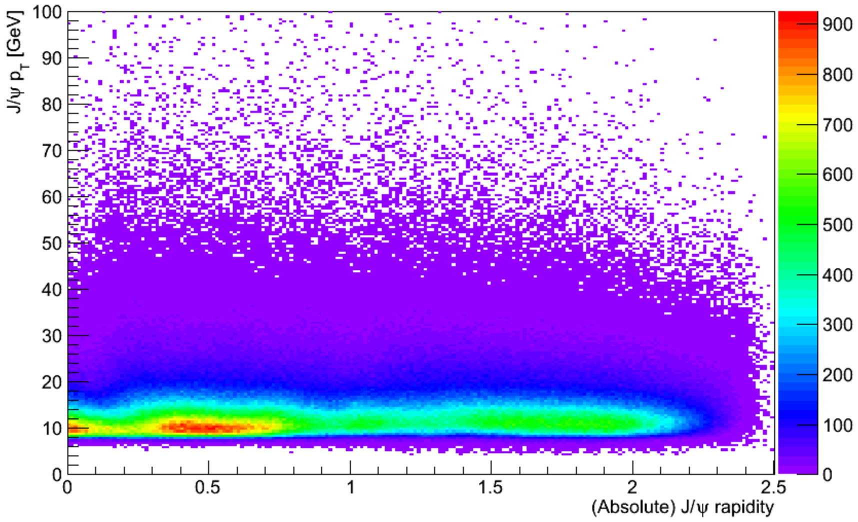

Figure 4.7: Distribution of J/ψ candidates as a function of J/ψ p_T and rapidity with the invariant mass cut $\pm$ 400 MeV within the J/ψ PDG mass. The events are not weighted.

The invariant mass distribution of the $J/\psi \rightarrow \mu^+\mu^-$ candidates in each bin is fit by RooFit [43] using a binned maximum likelihood method. Because the intrinsic widths of the J/ψ and $\psi(2S)$ are much smaller than the detector resolution, the signals of J/ψ and $\psi(2S)$ are presumed to be Gaussians $G(m, \sigma)$. The background is described by an exponential function $Exp(\lambda)$. Thus, the resulting likelihood function takes the following form

$$L = N_{J/\psi} \cdot G_{J/\psi}(m_{J/\psi}, \sigma_{J/\psi}) + N_{\psi(2S)} \cdot G_{\psi(2S)}(m_{\psi(2S)}, \sigma_{\psi(2S)}) + N_{bkg} \cdot Exp(\lambda), \tag{4.8}$$

where $N_{J/\psi}$, $N_{\psi(2S)}$ and N_{bkg} are real coefficients. Because the resolution of the detector is similar for both J/ψ and $\psi(2S)$, the $\sigma_{J/\psi} = \sigma_{\psi(2S)}$ was chosen. The PDG values of J/ψ and $\psi(2S)$ masses were fixed to reduce the additional degree of freedom of the likelihood function.

Each J/ψ candidate is weighted by a weight w defined in equation 4.5. The invariant mass distributions with fits for all bins are shown in figures 4.8 $-$ 4.11. The fit parameters are included in appendix A. The result of the fit is used to determine the inclusive differential production cross-section for each bin.

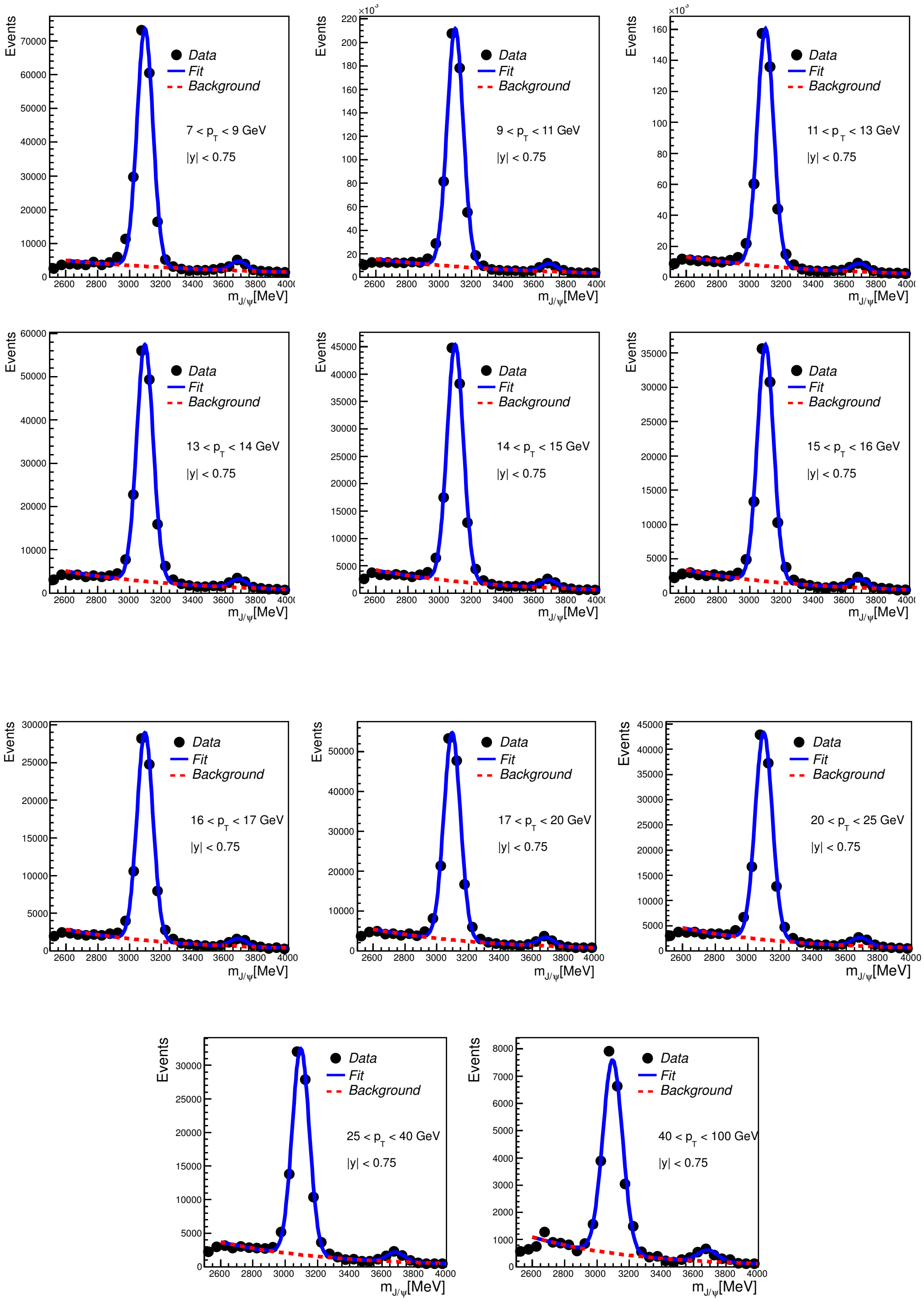

Figure 4.8: Invariant mass distribution of corrected di-muon candidates in rapidity $|y| < 0.75$ for different intervals of transverse momenta.

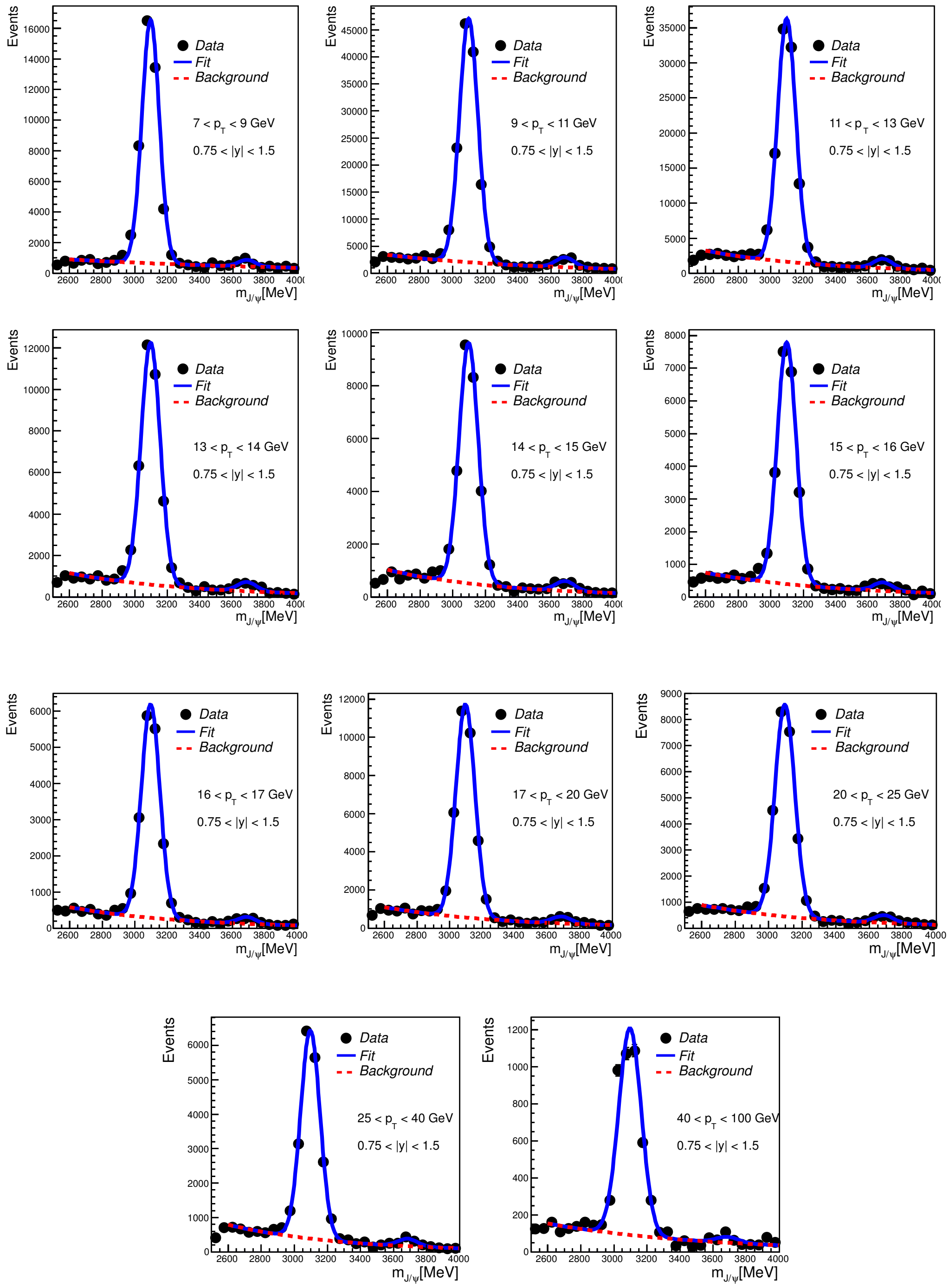

Figure 4.9: Invariant mass distribution of corrected di-muon candidates in rapidity $0.75 < |y| < 1.5$ for different intervals of transverse momenta.

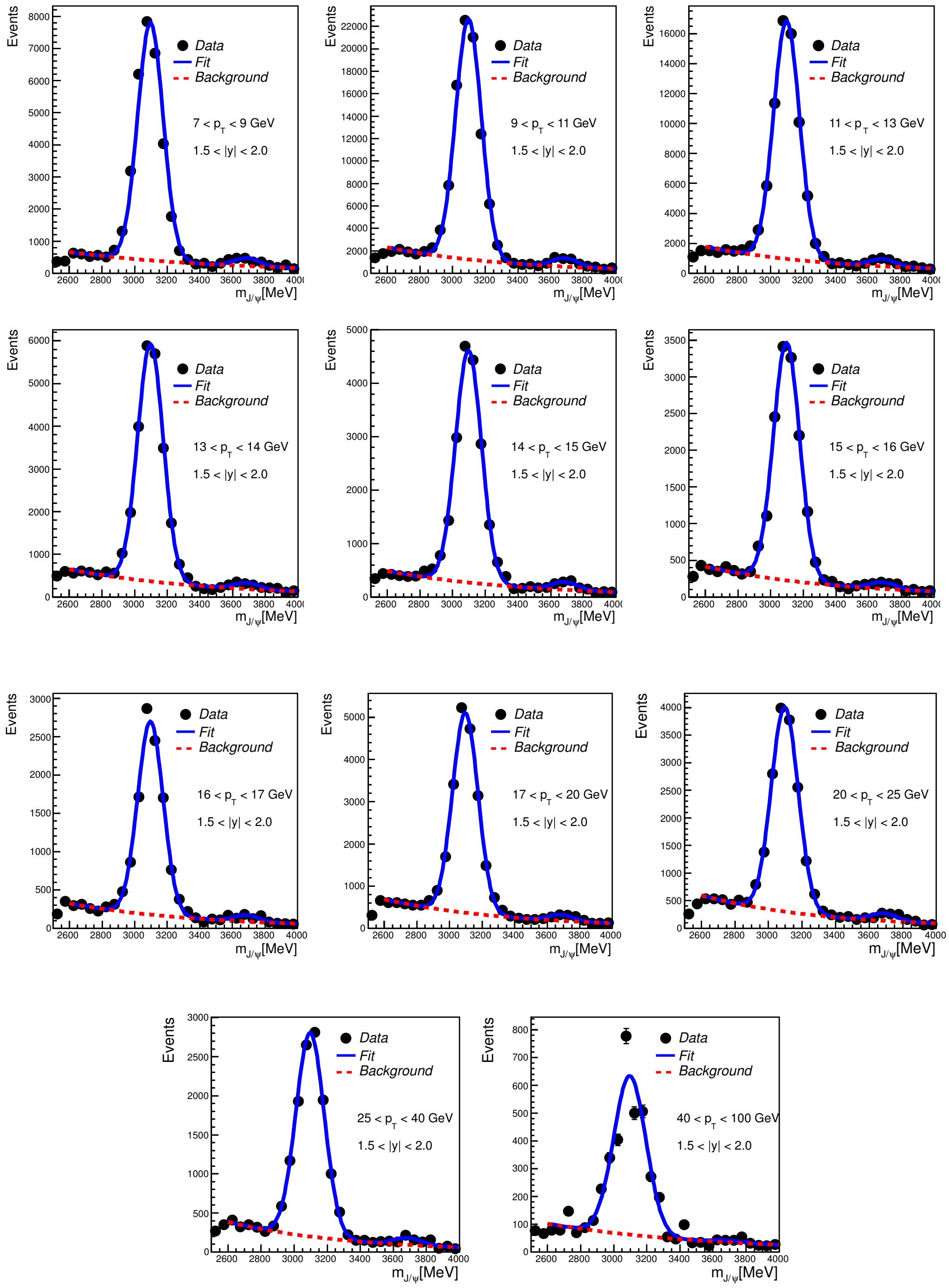

Figure 4.10: Invariant mass distribution of corrected di-muon candidates in rapidity $1.5 < |y| < 2.0$ for different intervals of transverse momenta.

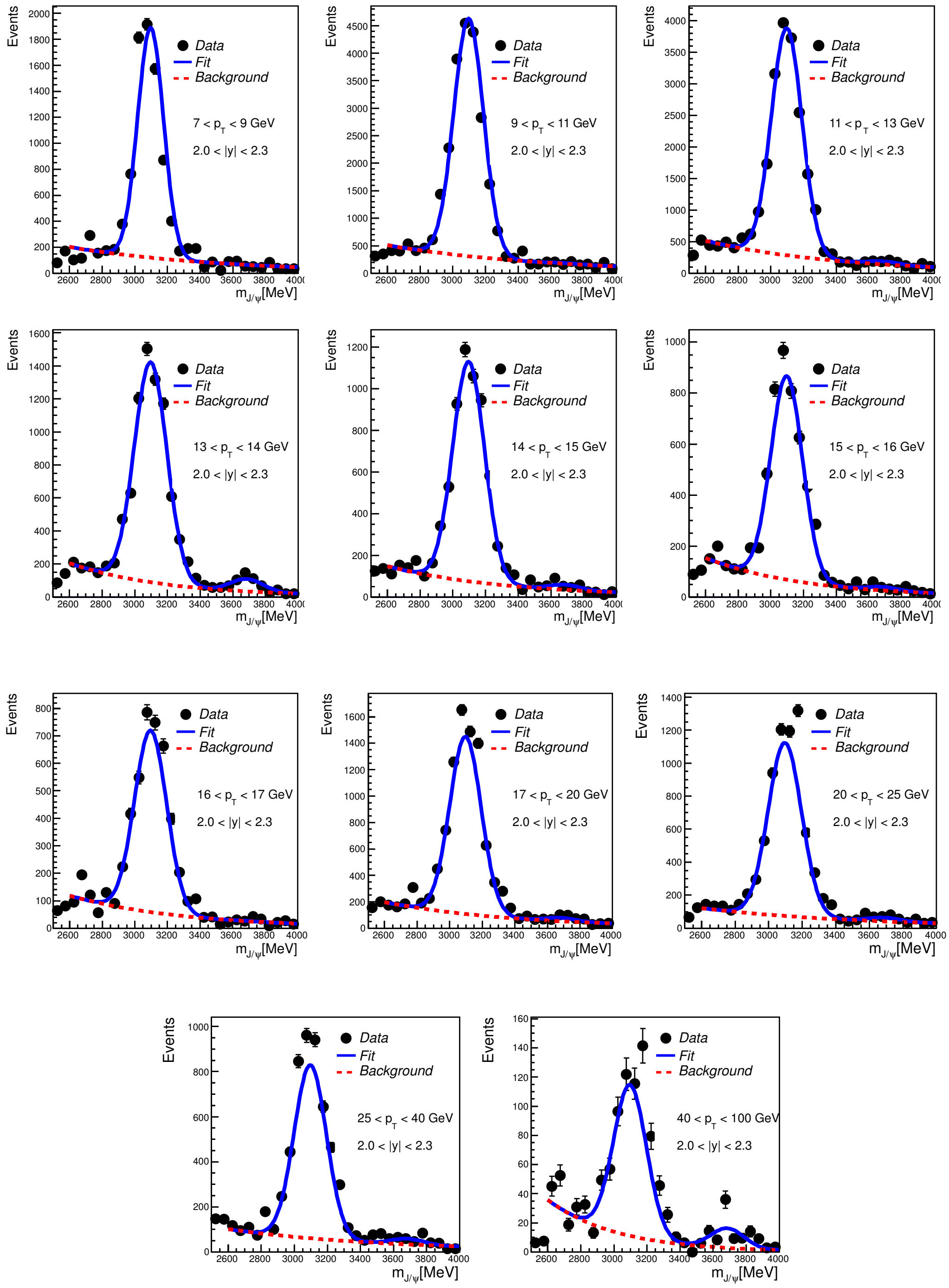

Figure 4.11: Invariant mass distribution of corrected di-muon candidates in rapidity $2.0 < |y| < 2.3$ for different intervals of transverse momenta.

4.4.3 Uncertainties

We consider the following sources of the systematic uncertainty of the J/ψ differential cross section: luminosity determination, reconstruction and trigger efficiencies. To simplify, we consider the systematic uncertainties not correlated.

A preliminary value of the relative luminosity uncertainty is determined to be 3.6 % and is described in more detail in [34].

The trigger efficiency and single muon reconstruction maps were computed from the Monte Carlo data using tag and probe method. The value of systematic uncertainty for a single muon reconstruction is delivered with maps for each pseudorapidity and p_T bin in a form of $\pm 1\ \sigma$ maps. The systematic uncertainty for the trigger efficiency is contained in the di-muon correction factor $c_{\mu\mu}$. This factor for trigger efficiency is slightly modified for both $+1\ \sigma$ and $-1\ \sigma$. Due to these modified maps and factors, the value of weight factor w (4.5) is changed. Using this changed weight factor we produce new histograms, where each event is weighted by a modified weight factor. We use the same algorithms for the J/ψ mass distribution fit and a slightly different result is obtained. A relative deviation between the results is presented as a systematic uncertainty. This procedure is used for each weight factor separately.

We also consider the statistical uncertainty, which is determined as the uncertainty from the likelihood fit. The summary of uncertainties for each p_t and rapidity bin is shown in figure 4.12. The systematic uncertainty due to luminosity (3.6 %) is not shown, because this uncertainty is constant for all bins, but it is included in the total uncertainty.

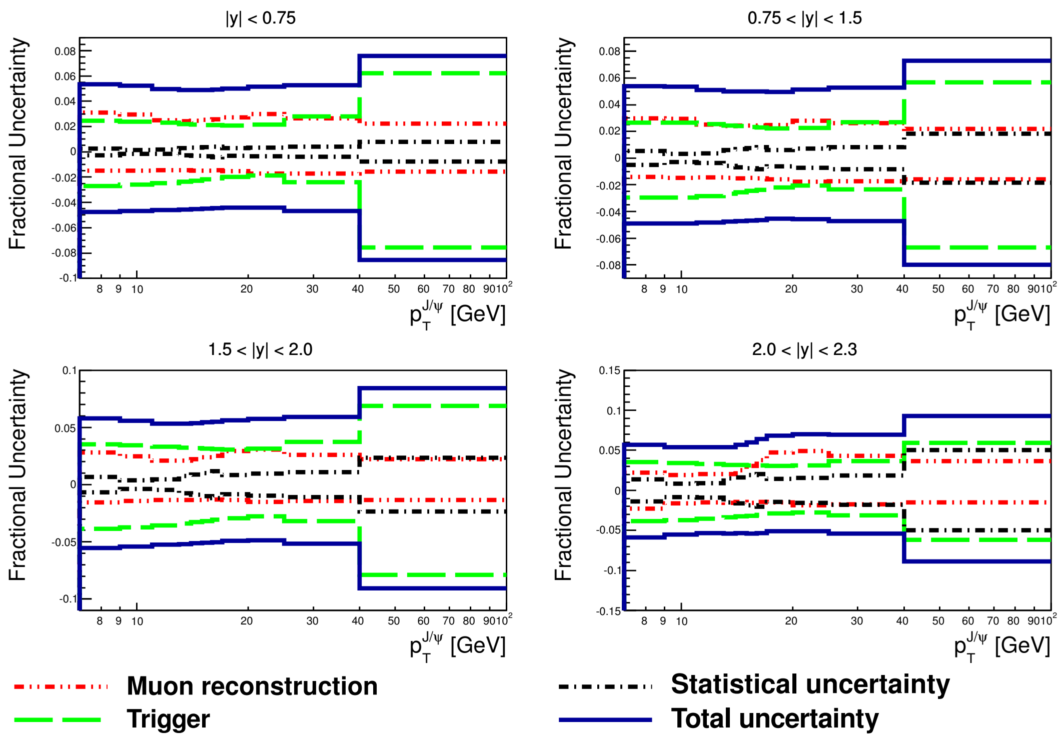

Figure 4.12: Summary of the contributions from multiple sources of the total uncertainty of the inclusive differential cross section in the transverse momentum and rapidity bins. The luminosity uncertainty is not plotted separately, but is included in the total uncertainty.

The J/ψ polarization, which is not taken into account, may have additional impact on the kinematic acceptance of the detector. The kinematic acceptance is a probability that the muons from a J/ψ with transverse momentum p_T and rapidity y fall into the fiducial volume of the detector. The polarization of J/ψ is highly correlated with reconstruction efficiency and from theory it has a nonzero value.

4.4.4 Results of inclusive J/ψ cross section

The results of the inclusive fiducial differential cross section are presented in figure 4.13.

The differential cross section is limited in the low p_T region due to the selected trigger with a 4 GeV muon threshold. In the region of J/ψ transverse momentum from 4 GeV to 7 GeV, only few events were observed, and the invariant mass fit could not be performed. Thus, the results are plotted for a J/ψ p_T of 7 GeV and further. In order to compare the results to the 2010 data at 7 TeV, the kinematic acceptance correction would have to be added.

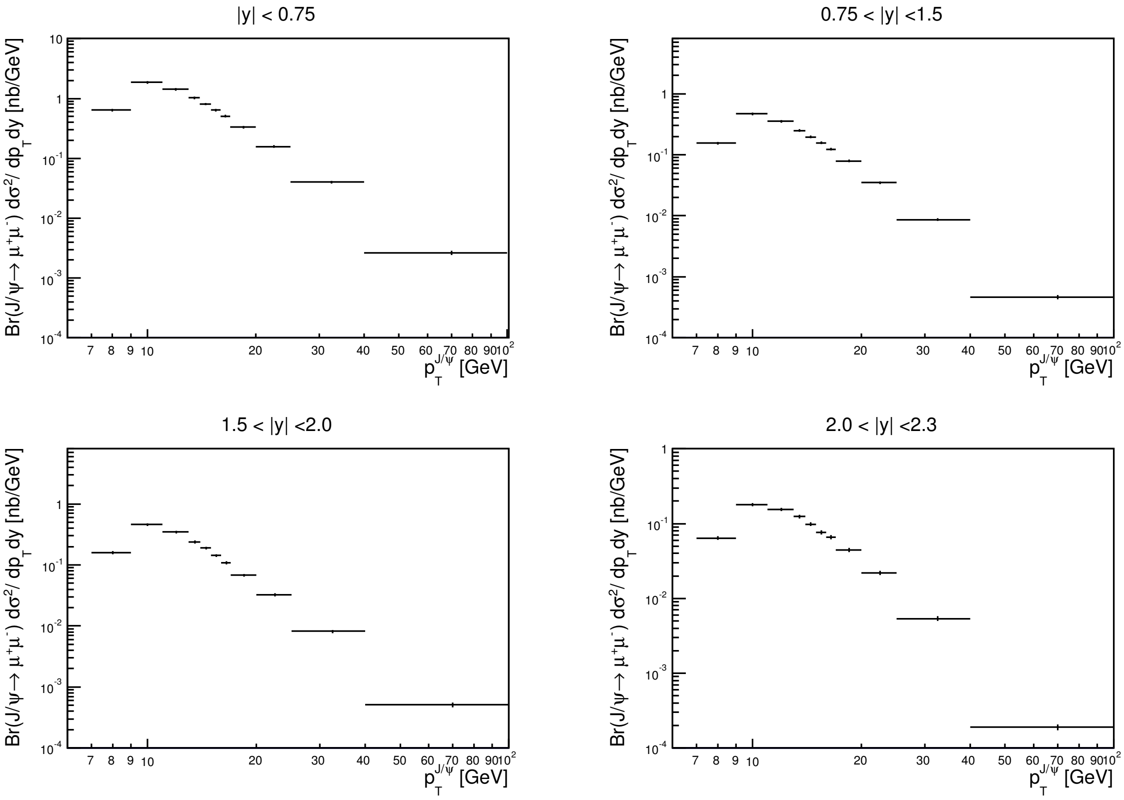

Figure 4.13: The obtained inclusive fiducial cross section in four ranges of rapidity.

4.5 Measurement of the Non-Prompt J/ψ Fraction

The J/ψ production mechanism at hadron a collider can be categorized into three groups:

- Prompt J/ψ produced directly in a proton-proton collision.
- Prompt J/ψ produced indirectly (via decay of heavier charmonium states such as χ_{c_J}).
- Non-Prompt J/ψ from the decay of a B-hadron. These J/ψ candidates are usually produced and decay at a B-hadron displaced secondary vertex.

The prompt decays occur very close to the primary vertex of the parent proton-proton collision. The non-prompt decays occur at a greater distance, typically O(100) μm, due to the long lifetime of their B-hadron parent. The measurement of the fraction of the J/ψ yield coming from B-hadron decays, f_B, relies on the discrimination of J/ψ mesons produced at a distance from the pp collision vertex. As a discrimination variable, pseudo-proper lifetime is used.

Pseudo-proper lifetime

The pseudo-proper lifetime τ is defined as a lifetime in a transverse plane and can be determined from the following equation:

$$\tau = \frac{L_{xy} m_{PDG}^{J/\psi}}{p_T^{J/\psi}}, \tag{4.9}$$

where the L_{xy} is the signed projection of the J/ψ decay vertex, $\vec{L}$, onto its transverse momentum, $\vec{p}_T^{J/\psi}$. The PDG value of J/ψ mass $m_{PDG}^{J/\psi}$ is used to reduce the correlation between the fits that will be performed on the lifetime.

4.5.1 Fit of J/ψ candidates pseudo-proper time

At first, only the J/ψ candidates with invariant mass in range 3 σ around J/ψ PDG mass are used [4]. The pseudo-proper time is fitted bin by bin. Bins are divided in p_T and rapidity with the same step size as for inclusive fiducial differential production cross-section. The pseudo-proper time in each bin is fitted with a likelihood function

$$L = f_{bkg} \cdot F_{bkg} + (1 - f_{bkg}) \cdot F_{sig}, \tag{4.10}$$

where f_{bkg} is a fraction of the background component and F_{bkg} and F_{sig} are functions describing the distribution of background and signal, respectively. The signal distribution is composed of a prompt and non-prompt component and may be described as,

$$F_{sig} = f_B \cdot F_B + (1 - f_B) \cdot F_p, \tag{4.11}$$

where f_B is a fraction of J/ψ from B-hadron decays, and F_B and F_p are the pseudo-proper time distributions for the prompt and non-prompt J/ψ, respectively.

The pseudo-proper time distribution of the J/ψ particles from B-hadron decays is an exponential function convolved with the pseudo-proper time resolution $R(\sigma)$,

$$F_B = R(\sigma) \otimes e^{-\frac{\tau}{\tau_{eff}}}. \tag{4.12}$$

The pseudo-proper time resolution $R(\sigma)$ is modeled with a Gaussian distribution centered at $\tau = 0$.

For a direct production of the J/ψ signal, the pseudo-proper time is the Dirac distribution convolved with the pseudo-proper time resolution $R(\sigma)$,

$$F_p = R(\sigma) \otimes \delta. \tag{4.13}$$

The pseudo-proper time distribution for the background component was modeled as a sum of two decays described with an exponential function convolved with the Gaussian resolution function $R^{1,2}_{bkg}$ and a prompt component modeled by a delta function convolved with the Gaussian resolution R^1_{bkg},

$$F_{bkg} = R^1_{bkg}(\sigma_1) \otimes [a_1 \cdot e^{-\frac{\tau}{\tau_{bkg1}}} + (1 - a_1 - a_2)\delta(\tau)] + a_2 \cdot R^2_{bkg}(\sigma_2) \otimes e^{-\frac{\tau}{\tau_{bkg2}}}. \tag{4.14}$$

The R^1_{bkg} and R^2_{bkg} are centered at $\tau = 0$, but they have a different standard deviation.

The shape and parameters of the background distribution are acquired from the fit of the lifetime distribution in the sidebands, i.e. outside of the J/ψ and $\psi(2S)$ invariant mass peaks. This procedure is called a data-driven background estimation technique. The invariant mass windows for the background were chosen to be $2500 - 2800$ MeV, $3400 - 3500$ MeV and $3850 - 4300$ MeV. It is assumed, that the background under the signal peaks has the same shape as outside of the signal peaks. The resulting lifetime distribution of the background with fit parameters is shown in figure 4.14.

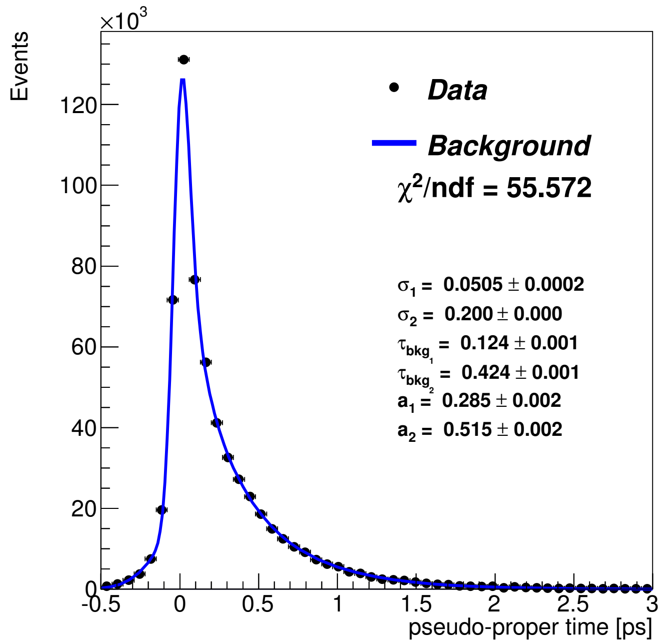

Figure 4.14: Lifetime distribution of the background events outside the J/ψ and $\psi(2S)$ peaks in the dimuon invariant mass ranges $2500-2800$ MeV, $3400-3500$ MeV and $3850-4300$ MeV with fit parameters and χ^2.

The fraction of the background component in a lifetime distribution is acquired from the invariant mass fit for each pseudorapidity and transverse momentum bin made in subsection 4.4.2. Thus, we have only three free parameters in the lifetime distribution namely σ, τ and f_B.

All bins with fits are shown in Figures 4.15 – 4.18. The list of all fit parameters can be found in appendix C.

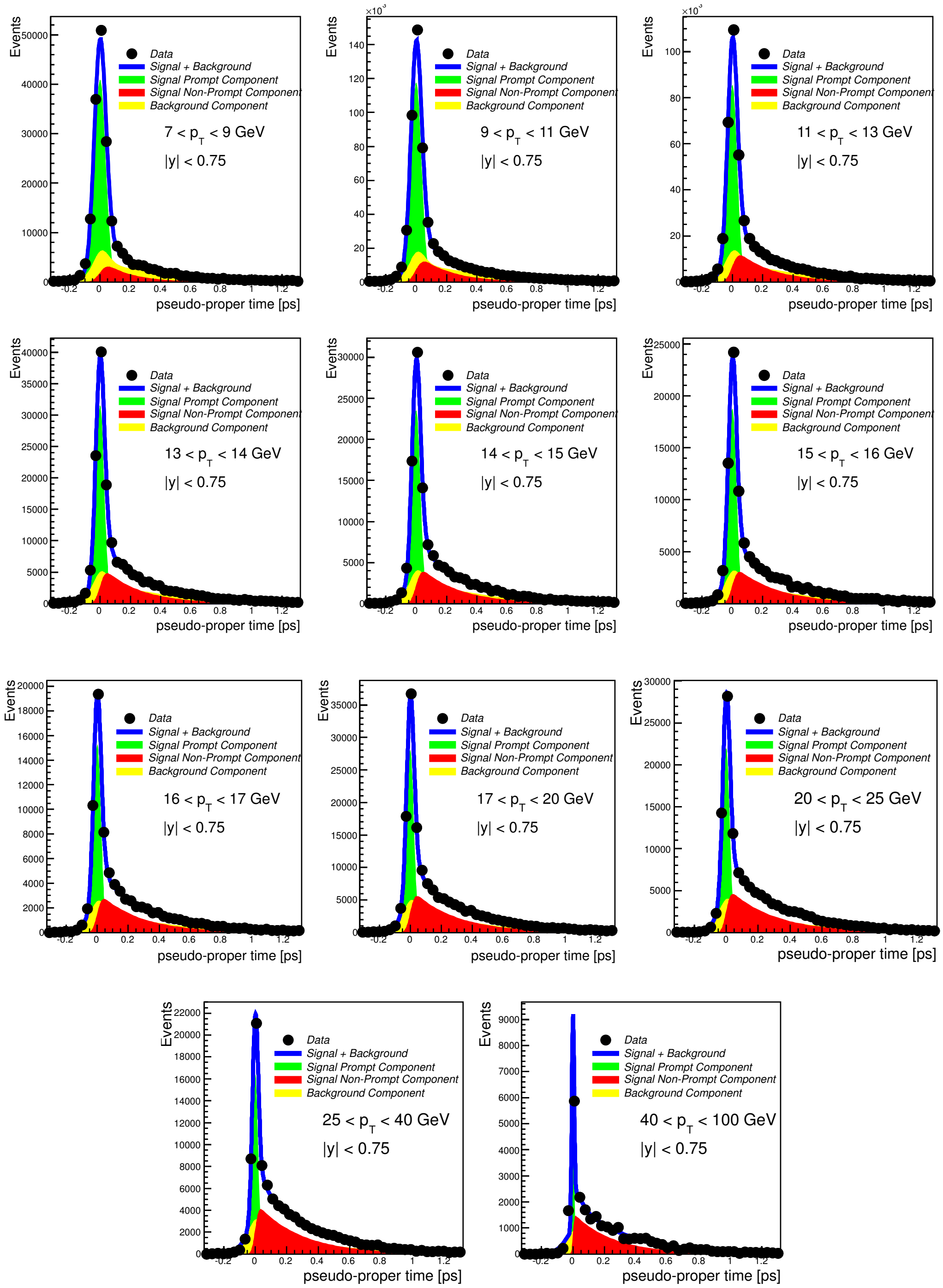

Figure 4.15: The pseudo-proper time distributions for rapidity $|y| < 0.75$ for different intervals of transverse momenta. The data are fitted with three components: prompt, non-prompt and background.

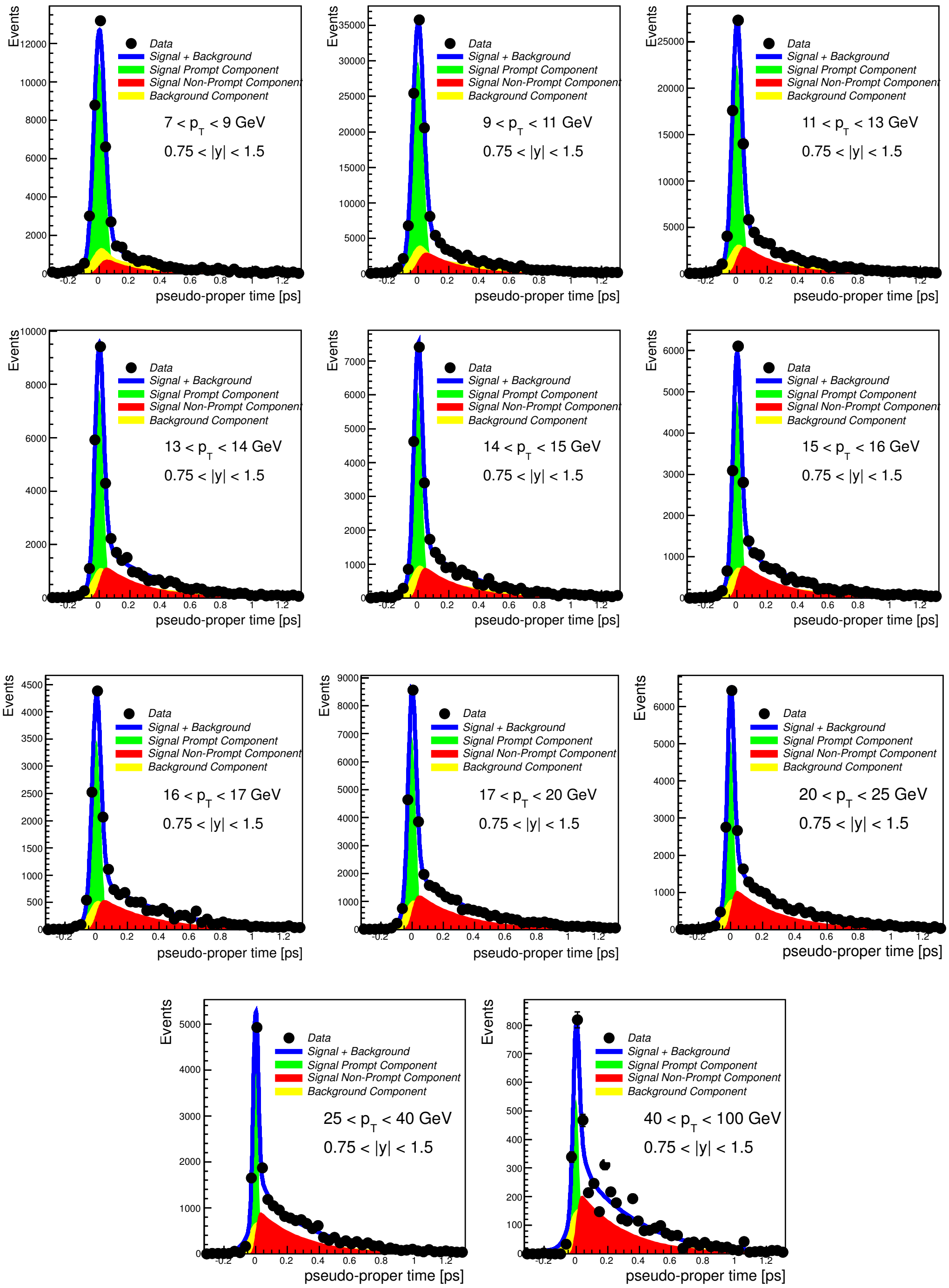

Figure 4.16: The pseudo-proper time distributions for rapidity $0.75 < |y| < 1.5$ for different intervals of transverse momenta. The data are fitted with three components: prompt, non-prompt and background.

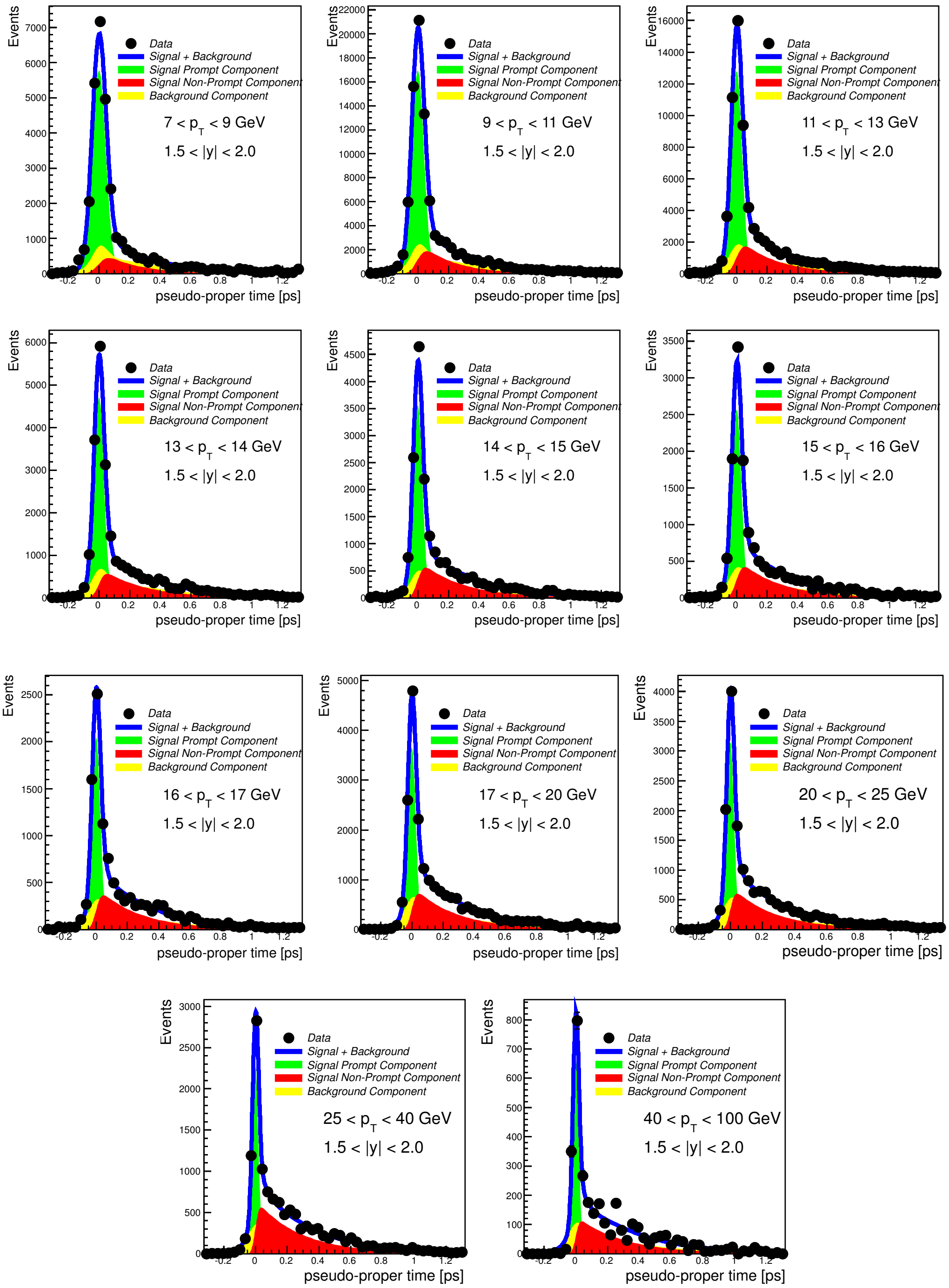

Figure 4.17: The pseudo-proper time distributions for rapidity $1.5 < |y| < 2.0$ for different intervals of transverse momenta. The data are fitted with three components: prompt, non-prompt and background.

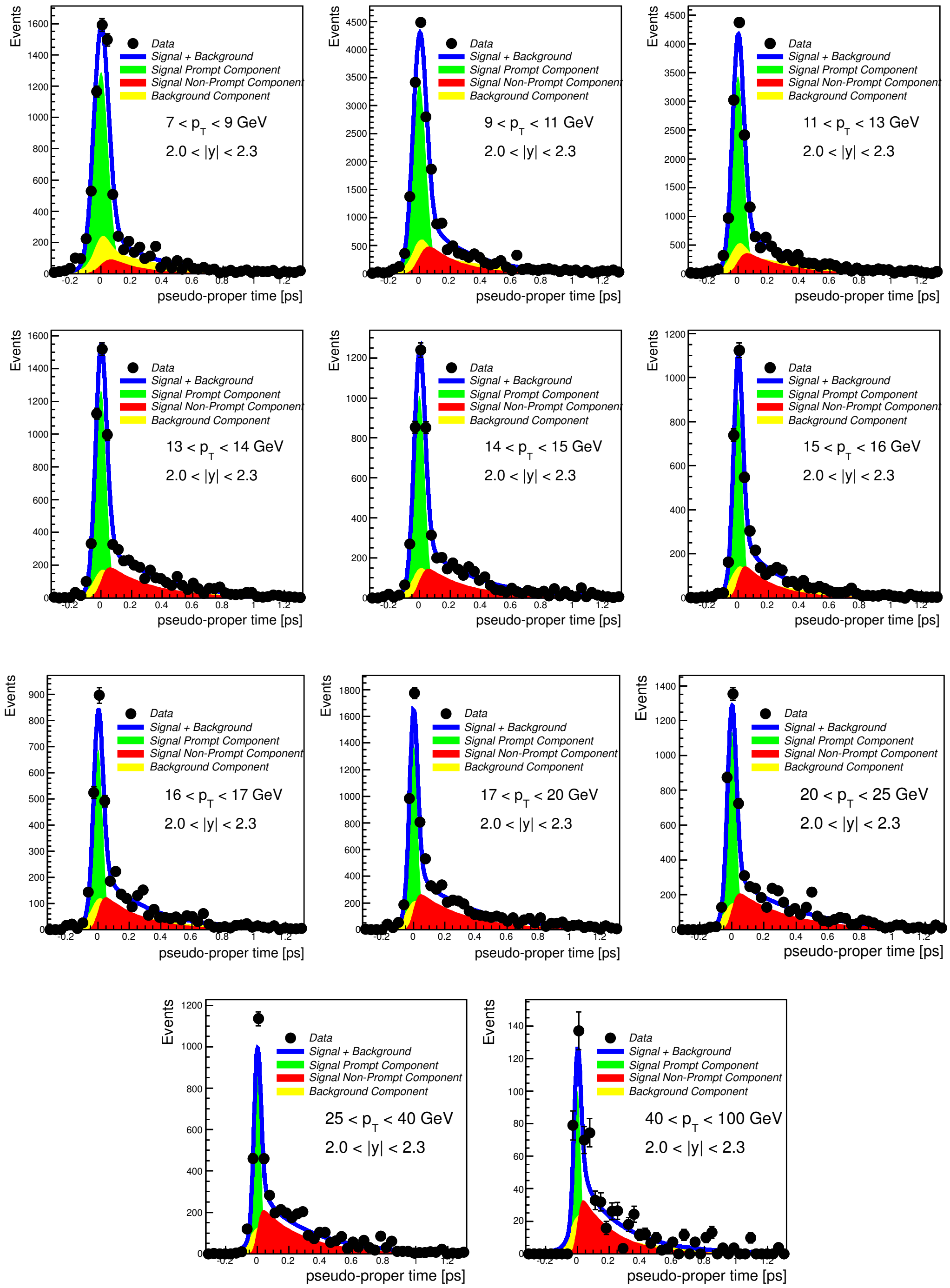

Figure 4.18: The pseudo-proper time distributions for rapidity $2.0 < |y| < 2.3$ for different intervals of transverse momenta. The data are fitted with three components: prompt, non-prompt and background.

4.5.2 Uncertainties

We consider the following sources of the systematic uncertainty on the non-prompt J/ψ production fraction: background estimation, reconstruction and trigger efficiencies. To simplify, we consider that the systematic uncertainties are not correlated.

The systematic uncertainties derived from trigger and reconstruction efficiencies are computed in the same way as in subsection 4.4.3. In addition, the systematic uncertainty from determination of background to signal ratio is assumed. This systematic uncertainty was obtained by using a statistical uncertainty of the background to signal ratio and by computing the J/ψ lifetime fit with modified parameters. The maximal relative deviation is used as a systematic uncertainty for the background estimation. The summary of uncertainties for each p_t and rapidity bin is shown in figure 4.19.

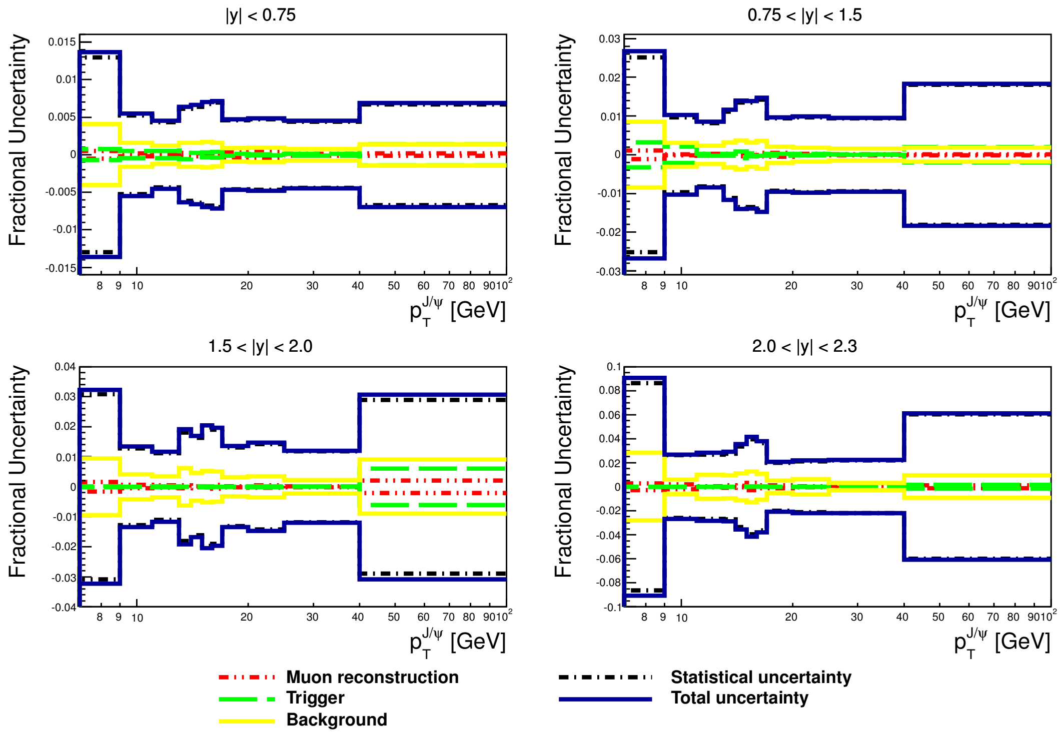

Figure 4.19: Summary of the contribution from multiple sources of the total uncertainty of the non-prompt J/ψ production fraction.

4.5.3 Results of the non-prompt J/ψ production fraction fit

The results of the non-prompt J/ψ production fraction in four measured rapidity bins can be seen in figure 4.20. The data are compared with the results of ATLAS collaboration [42], where the same binning was chosen.

A strong dependency of the non-prompt fraction on J/ψ p_T is observed. With increasing p_T, the probability of production of J/ψ from B mesons rises. The dependency of the non-prompt fraction on rapidity is not significant. The results are in a good agreement with the ATLAS results.

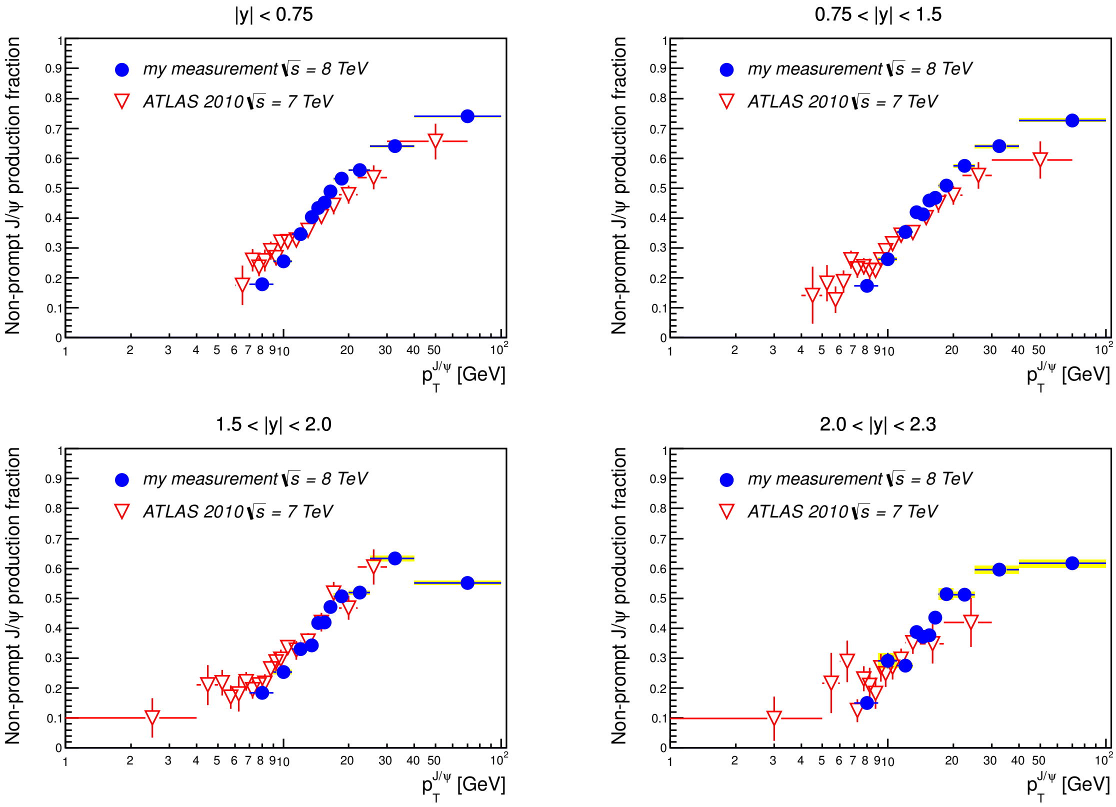

Figure 4.20: The fraction of J/ψ produced indirectly from the decay of B meson to all J/ψ in pp collision. The data are compared with an equivalent result from ATLAS at $\sqrt{s} = 7$ TeV [42].

4.6 J/ψ differential production cross-section compared to Monte Carlo

The prompt and non-prompt J/ψ differential production cross-section was produced using the simulated MC data. The MC samples have undergone the same analysis path with identical cuts as the real data. The same procedure as for the real data, described in section 4.4, was used to determine the differential production cross-section. Because the MC data were reconstructed by the same algorithms, we can also use the same trigger selection and reconstruction efficiency maps.

The resulting differential production cross-sections were reweighted on the same workspace as the cross section determined from the data. To compare the results obtained from the data and MC, the prompt (P) and non-prompt (B) cross sections were summed in the ratio of non-prompt to prompt fraction f_B in each bin.

$$\left(\frac{d^2\sigma}{dp_T dy}\right)_{\mathrm{MC}} = f_B \cdot \left(\frac{d^2\sigma}{dp_T dy}\right)_{\mathrm{B}} + (1 - f_B) \cdot \left(\frac{d^2\sigma}{dp_T dy}\right)_{\mathrm{P}} \tag{4.15}$$

The fraction f_B was computed in section 4.5 and is derived from the data. The results depicting the data to MC ratios are shown in figure 4.21.

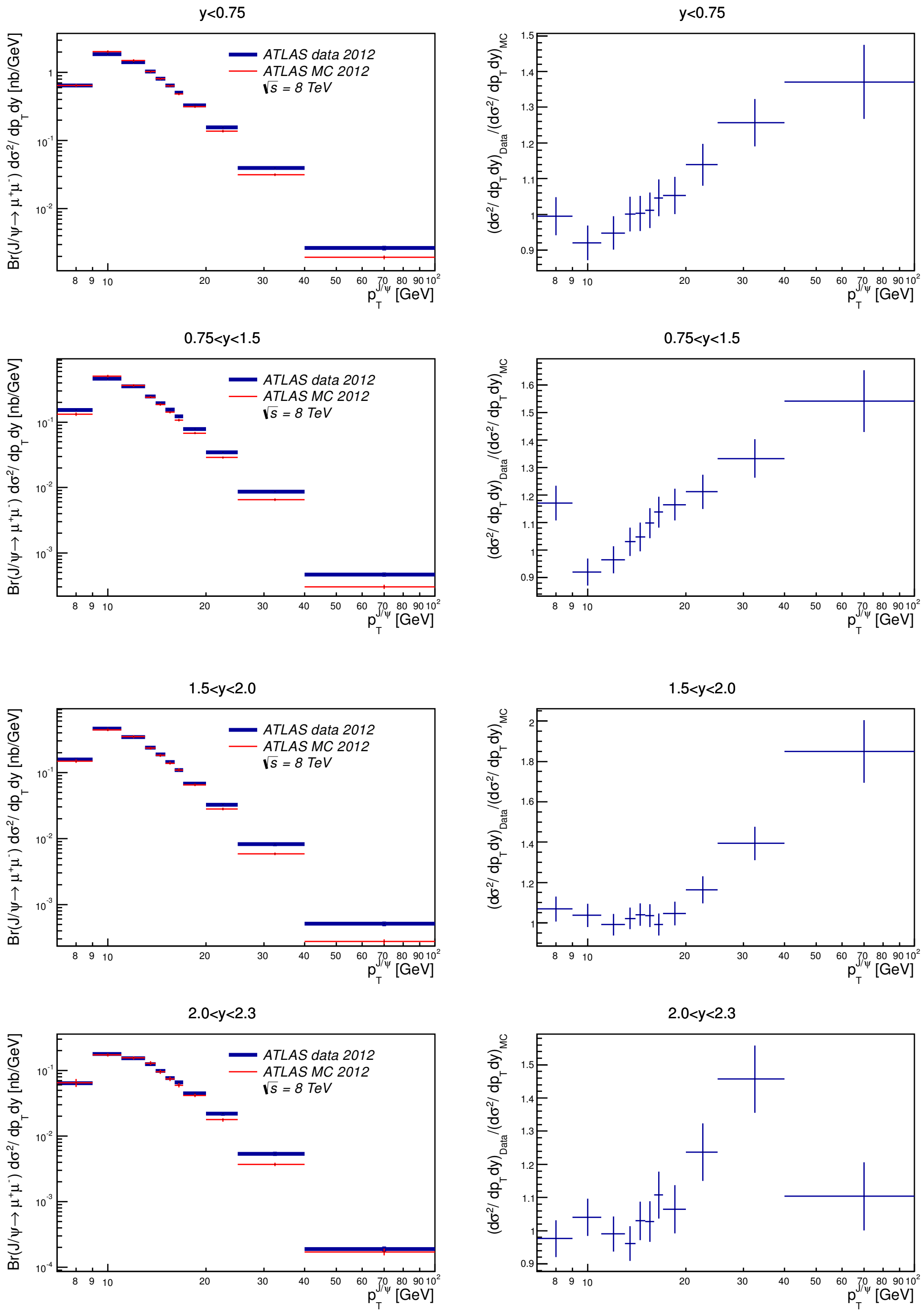

Figure 4.21: On the left side, the measured cross sections are compared to the cross sections obtained from the MC. On the right side, the data to MC ratios are shown. The MC has been reweighted on the same workspace as the cross section determined from the data.

The results from the MC compare very well to the measured data in the low p_T region, the data to MC ratio ranges are from 0.9 to 1.2. At higher p_T, independently on rapidity, the MC underestimates the data. This is probably due to more J/ψ production mechanisms than the mechanisms considered, such as $Z \to BB$ or $H \to BB$ and the effects of pileup.

Chapter 5

Conclusions

This thesis was devoted to a study of quarkonia states, particularly the J/ψ resonance. The primary objective was the measurement of the inclusive fiducial $J/\psi \to \mu^+\mu^-$ differential production cross-section in proton-proton collisions at the centre of mass energy $\sqrt{s} = 8$ TeV, as well as the measurement of the fraction of J/ψ mesons produced via decay of B mesons. For this purpose, the data from periods E and G in the ATLAS 2012 run at $\sqrt{s}$ =8 TeV were used. The Monte Carlo simulations of directly and indirectly produced J/ψ mesons are compared to the measured data.

In the last chapter which describes my own analysis of the experimental data, the data flow and acquired results are presented. The fractions of indirectly produced J/ψ mesons are compared to the results of the ATLAS 2010 data analysis at $\sqrt{s}$ =7 TeV, while the inclusive fiducial cross sections are compared to the Monte Carlo data samples. Both results are in good agreement, especially in low transverse momenta regions, when considering that no corrections for detector acceptance were made. Due to larger statistics available in 2012 ATLAS run, the p_T range was extended to reach higher p_T region than was measured anywhere before. To improve the results, data have to be corrected for the detector acceptance and other effects which can affect the measured results. This will be the objective of my further studies.

Appendix A

List of J/ψ invariant mass distribution parameters

	p_T [GeV]	$N_{J/\psi} \cdot 10^3$	$N_{\psi(2S)} \cdot 10^3$	$N_{bkg} \cdot 10^3$	σ	$\lambda \cdot 10^{-3}$	χ^2/ndf
$\lvert y\rvert < 0.75$	7−9	176.1±0.5	7.2±0.1	90.5±0.4	49.9±0.1	-0.86±0.01	360.82
	9−11	513.0±0.8	16.7±0.2	257.5±0.7	50.5±0.1	-1.07±0.01	516.59
	11−13	389.3±0.7	13.6±0.2	205.1±0.6	50.7±0.1	-1.22±0.01	359.17
	13−14	141.2±0.4	5.1±0.1	78.2±0.4	51.6±0.1	-1.24±0.01	130.80
	14−15	110.8±0.4	3.67±0.10	62.5±0.3	51.1±0.2	-1.34±0.01	96.27
	15−16	87.9±0.3	3.40±0.09	49.8±0.3	50.9±0.2	-1.35±0.01	83.61
	16−17	69.5±0.3	2.62±0.08	40.5±0.3	50.3±0.2	-1.43±0.02	72.27
	17−20	136.4±0.4	5.6±0.1	79.5±0.4	52.3±0.2	-1.37±0.01	102.20
	20−25	107.3±0.4	4.3±0.1	64.7±0.3	52.1±0.2	-1.43±0.01	105.87
	25−40	82.2±0.3	3.82±0.09	52.3±0.3	53.4±0.2	-1.44±0.01	55.38
	40−100	21.8±0.2	1.30±0.06	14.8±0.2	61.3±0.4	-1.57±0.03	29.94
$0.75 < \lvert y\rvert < 1.5$	7−9	42.4±0.2	1.15±0.06	18.4±0.2	53.2±0.3	-0.66±0.02	91.55
	9−11	128.2±0.4	5.2±0.1	57.5±0.3	56.8±0.2	-1.04±0.01	80.60
	11−13	97.4±0.3	3.77±0.09	47.1±0.3	56.0±0.2	-1.37±0.02	48.21
	13−14	34.3±0.2	1.31±0.06	17.2±0.2	58.7±0.3	-1.31±0.03	26.89
	14−15	26.8±0.2	1.13±0.05	14.9±0.2	58.8±0.4	-1.39±0.03	18.68
	15−16	21.5±0.2	0.76±0.05	11.4±0.1	57.9±0.4	-1.28±0.03	17.34
	16−17	16.9±0.1	0.53±0.04	8.3±0.1	57.1±0.4	-1.43±0.04	9.11
	17−20	32.6±0.2	1.07±0.05	16.2±0.2	58.3±0.3	-1.36±0.03	13.60
	20−25	23.9±0.2	0.88±0.05	13.0±0.2	58.7±0.4	-1.37±0.03	13.23
	25−40	17.8±0.1	0.64±0.04	11.2±0.1	58.8±0.5	-1.43±0.03	10.90
	40−100	3.83±0.07	0.11±0.02	2.59±0.07	69±1	-1.03±0.06	11.51

Table A.1: The fit parameters with statistical uncertainties of J/ψ distribution in the rapidity bins $|y| < 0.75$ and $0.75 < |y| < 1.5$.

	p_T [GeV]	$N_{J/\psi} \cdot 10^3$	$N_{\psi(2S)} \cdot 10^3$	$N_{bkg} \cdot 10^3$	σ	$\lambda \cdot 10^{-3}$	χ^2/ndf
$1.5 < \lvert y \rvert < 2.0$	7−9	28.9±0.2	1.00±0.06	11.4±0.2	78.0±0.5	-1.00±0.03	35.61
	9−11	83.9±0.3	3.00±0.10	35.3±0.3	78.2±0.3	-1.25±0.02	32.10
	11−13	63.2±0.3	1.95±0.09	27.4±0.3	79.5±0.3	-1.23±0.02	14.19
	13−14	21.8±0.2	0.57±0.05	10.4±0.2	78.3±0.6	-1.14±0.03	6.95
	14−15	17.3±0.2	0.59±0.05	7.7±0.1	79.3±0.7	-1.19±0.04	9.03
	15−16	13.1±0.1	0.37±0.04	6.5±0.1	80.5±0.7	-1.22±0.04	4.51
	16−17	9.9±0.1	0.33±0.04	5.0±0.1	78.3±0.9	-1.22±0.05	6.31
	17−20	18.6±0.2	0.57±0.05	10.5±0.2	78.2±0.7	-1.25±0.04	5.32
	20−25	14.8±0.1	0.55±0.05	8.7±0.1	79.9±0.7	-1.37±0.04	6.25
	25−40	11.2±0.1	0.39±0.04	5.7±0.1	85.7±0.9	-1.34±0.05	4.87
	40−100	2.79±0.07	0.04±0.02	1.75±0.07	98±2	-0.99±0.09	9.32
$2.0 < \lvert y \rvert < 2.3$	7−9	7.01±0.10	0.00±0.02	3.40±0.08	79±1	-1.05±0.05	39.37
	9−11	19.7±0.2	0.06±0.05	8.8±0.2	90.9±0.7	-1.00±0.04	23.95
	11−13	16.9±0.2	0.23±0.05	8.1±0.2	93.9±0.8	-1.19±0.04	10.18
	13−14	6.83±0.10	0.39±0.03	2.73±0.10	100±5	-1.66±0.09	5.56
	14−15	5.38±0.09	0.12±0.03	2.29±0.09	97±1	-1.34±0.08	7.04
	15−16	4.18±0.08	0.07±0.03	2.16±0.08	97±2	-1.65±0.10	6.57
	16−17	3.61±0.07	0.01±0.02	1.87±0.07	99±2	-1.41±0.09	10.34
	17−20	7.3±0.1	0.14±0.03	3.5±0.1	97±1	-1.23±0.07	13.68
	20−25	6.02±0.09	0.13±0.03	2.41±0.09	100±1	-0.99±0.08	13.55
	25−40	4.42±0.08	0.15±0.03	2.01±0.09	98±2	-1.02±0.09	12.02
	40−100	0.62±0.03	0.08±0.01	0.45±0.03	100±1	-2.3±0.3	4.8

Table A.2: The fit with statistical uncertainties parameters of J/ψ distribution in the rapidity bins $1.5 < |y| < 2.0$ and $2.0 < |y| < 2.3$.

Appendix B

Inclusive $J/\psi \to \mu^+\mu^-$ production cross section results

$\frac{d^2\sigma}{dydp_T}Br(J/\psi \to \mu^+\mu^-)$ [nb/GeV]						
p_T [GeV]	value	$\pm$ (stat.)	$\pm$ (syst.)	value	$\pm$ (stat.)	$\pm$ (syst.)
	$\lvert y\rvert < 0.75$			$0.75 < \lvert y\rvert < 1.5$		
7−9	1.8682	±0.0091	$^{+0.100}_{-0.089}$	0.4497	±0.0011	$^{+0.024}_{-0.022}$
9−11	5.441	±0.045	$^{+0.28}_{-0.26}$	1.3599	±0.0056	$^{+0.073}_{-0.066}$
11−13	4.130	±0.030	$^{+0.20}_{-0.19}$	1.0326	±0.0037	$^{+0.052}_{-0.050}$
13−14	2.996	±0.026	$^{+0.15}_{-0.14}$	0.7272	±0.0031	$^{+0.036}_{-0.034}$
14−15	2.350	±0.018	$^{+0.11}_{-0.11}$	0.5691	±0.0022	$^{+0.028}_{-0.027}$
15−16	1.864	±0.013	$^{+0.091}_{-0.083}$	0.4552	±0.0016	$^{+0.022}_{-0.021}$
16−17	1.4749	±0.0091	$^{+0.072}_{-0.065}$	0.3577	±0.0011	$^{+0.018}_{-0.016}$
17−20	0.9647	±0.0028	$^{+0.048}_{-0.042}$	0.23049	±0.00032	$^{+0.011}_{-0.010}$
20−25	0.45510	±0.00070	$^{+0.023}_{-0.020}$	0.101445	±0.000073	$^{+0.0052}_{-0.0046}$
25−40	0.116198	±0.000052	$^{+0.0061}_{-0.0054}$	0.0251768	±0.0000053	$^{+0.0013}_{-0.0012}$
40−100	0.00769564	±0.00000046	$^{+0.00058}_{-0.00066}$	0.001355539	±0.000000034	$^{+0.000096}_{-0.000105}$
	$1.5 < \lvert y\rvert < 2.0$			$2.0 < \lvert y\rvert < 2.3$		
7−9	0.4599	±0.0014	$^{+0.026}_{-0.025}$	0.18593	±0.00047	$^{+0.010}_{-0.011}$
9−11	1.3355	±0.0069	$^{+0.074}_{-0.072}$	0.5212	±0.0023	$^{+0.028}_{-0.028}$
11−13	1.0055	±0.0046	$^{+0.054}_{-0.053}$	0.4491	±0.0019	$^{+0.024}_{-0.024}$
13−14	0.6942	±0.0037	$^{+0.037}_{-0.036}$	0.3623	±0.0020	$^{+0.019}_{-0.019}$
14−15	0.5490	±0.0026	$^{+0.029}_{-0.028}$	0.2852	±0.0013	$^{+0.015}_{-0.014}$
15−16	0.4158	±0.0017	$^{+0.022}_{-0.021}$	0.22186	±0.00093	$^{+0.013}_{-0.011}$
16−17	0.3147	±0.0012	$^{+0.017}_{-0.015}$	0.19126	±0.00074	$^{+0.012}_{-0.009}$
17−20	0.19701	±0.00033	$^{+0.011}_{-0.010}$	0.12960	±0.00024	$^{+0.0087}_{-0.0063}$
20−25	0.094471	±0.000086	$^{+0.0054}_{-0.0045}$	0.063811	±0.000063	$^{+0.0044}_{-0.0031}$
25−40	0.0237570	±0.0000062	$^{+0.0014}_{-0.0012}$	0.0156388	±0.0000045	$^{+0.0010}_{-0.0008}$
40−100	0.001482529	±0.000000052	$^{+0.00012}_{-0.00013}$	0.000550038	±0.000000015	$^{+0.000043}_{-0.000040}$

Table B.1: The results of inclusive $J/\psi \to \mu^+\mu^-$ production cross section for each rapidity and p_T bin with systematical and statistical uncertainties.

Appendix C

List of J/ψ pseudo-proper time fit parameters

	p_T [GeV]	f_B	$\sigma \cdot 10^{-3}$	τ	χ^2/ndf		f_B	$\sigma \cdot 10^{-3}$	τ	χ^2/ndf
$\lvert y\rvert < 0.75$	7−9	0.179±0.002	37.8±0.1	0.184±0.002	37.494	$0.75 < \lvert y\rvert < 1.5$	0.173±0.004	35.1±0.2	0.192±0.005	30.349
	9−11	0.256±0.001	34.8±0.1	0.210±0.001	98.599		0.263±0.003	34.6±0.1	0.228±0.002	38.791
	11−13	0.346±0.002	31.6±0.1	0.234±0.001	86.004		0.354±0.003	29.9±0.2	0.245±0.002	26.878
	13−14	0.404±0.002	28.0±0.1	0.243±0.002	31.818		0.419±0.005	27.2±0.2	0.271±0.004	20.183
	14−15	0.434±0.003	27.7±0.2	0.256±0.002	38.070		0.412±0.006	26.9±0.3	0.257±0.004	23.936
	15−16	0.451±0.003	26.8±0.2	0.275±0.002	34.712		0.458±0.006	25.6±0.3	0.268±0.005	37.541
	16−17	0.489±0.003	24.1±0.2	0.266±0.002	29.763		0.467±0.007	27.4±0.4	0.322±0.006	19.688
	17−20	0.531±0.002	23.6±0.1	0.279±0.002	58.915		0.508±0.005	24.6±0.3	0.301±0.004	24.124
	20−25	0.561±0.003	22.0±0.1	0.285±0.002	79.265		0.574±0.006	20.8±0.3	0.293±0.004	34.802
	25−40	0.641±0.003	18.2±0.2	0.281±0.002	87.670		0.640±0.006	15.8±0.3	0.279±0.004	46.921
	40−100	0.739±0.005	7.4±0.1	0.252±0.003	79.371		0.73±0.01	19.0±0.7	0.291±0.009	8.864
$1.5 < \lvert y\rvert < 2.0$	7−9	0.183±0.006	45.0±0.4	0.224±0.007	22.780	$2.0 < \lvert y\rvert < 2.3$	0.15±0.01	48.2±0.9	0.19±0.01	14.74
	9−11	0.254±0.003	40.1±0.2	0.216±0.003	21.047		0.292±0.008	43.0±0.5	0.211±0.006	20.766
	11−13	0.330±0.004	35.4±0.2	0.242±0.003	11.558		0.276±0.007	36.7±0.4	0.250±0.007	11.614
	13−14	0.343±0.006	32.2±0.4	0.274±0.006	13.518		0.39±0.01	35.1±0.7	0.294±0.010	7.253
	14−15	0.418±0.007	30.1±0.4	0.273±0.006	16.539		0.37±0.01	35.2±0.7	0.28±0.01	7.19
	15−16	0.419±0.008	30.9±0.5	0.267±0.006	13.216		0.38±0.01	29.0±0.8	0.207±0.009	3.106
	16−17	0.472±0.009	26.5±0.5	0.270±0.007	5.963		0.44±0.02	29.3±0.8	0.24±0.01	5.79
	17−20	0.507±0.007	25.3±0.4	0.272±0.005	32.312		0.51±0.01	25.9±0.6	0.303±0.009	6.956
	20−25	0.519±0.007	22.9±0.4	0.267±0.005	21.298		0.51±0.01	26.8±0.6	0.324±0.010	11.603
	25−40	0.633±0.007	18.9±0.4	0.282±0.005	16.516		0.60±0.01	21.6±0.9	0.271±0.008	9.939
	40−100	0.55±0.02	18.6±0.7	0.30±0.01	17.42		0.62±0.04	21±2	0.21±0.02	3.48

Table C.1: The fit parameters with statistical uncertainties of J/ψ pseudo-proper time measurement for all slices of rapidity.

Appendix D

J/ψ non-prompt to inclusive production fraction results

p_T [GeV]	f_B	$\pm$ (stat.)	$\pm$ (syst.)	f_B	$\pm$ (stat.)	$\pm$ (syst.)
	$\lvert y\rvert < 0.75$			$0.75 < \lvert y\rvert < 1.5$		
7–9	0.1789	±0.0023	±0.00074	0.1729	±0.0043	±0.0016
9–11	0.2560	±0.0013	±0.00042	0.2634	±0.0025	±0.00098
11–13	0.3464	±0.0015	±0.00045	0.3536	±0.0029	±0.00083
13–14	0.4037	±0.0025	±0.00068	0.4188	±0.0047	±0.0014
14–15	0.4337	±0.0028	±0.00071	0.4115	±0.0056	±0.0016
15–16	0.4510	±0.0031	±0.00077	0.4578	±0.0062	±0.0015
16–17	0.4886	±0.0034	±0.00079	0.4673	±0.0067	±0.0017
17–20	0.5310	±0.0024	±0.00049	0.5082	±0.0047	±0.0011
20–25	0.5605	±0.0026	±0.00054	0.5738	±0.0055	±0.0010
25–40	0.6406	±0.0028	±0.00051	0.6400	±0.0060	±0.00100
40–100	0.7395	±0.0050	±0.0015	0.727	±0.013	±0.0019
	$1.5 < \lvert y\rvert < 2.0$			$2.0 < \lvert y\rvert < 2.3$		
7–9	0.1833	±0.0057	±0.0017	0.150	±0.013	±0.0042
9–11	0.2544	±0.0032	±0.0011	0.2917	±0.0076	±0.0018
11–13	0.3297	±0.0037	±0.0012	0.2757	±0.0073	±0.0028
13–14	0.3431	±0.0062	±0.0021	0.386	±0.011	±0.0037
14–15	0.4177	±0.0068	±0.0019	0.371	±0.012	±0.0042
15–16	0.4185	±0.0083	±0.0022	0.377	±0.015	±0.0048
16–17	0.4719	±0.0090	±0.0024	0.436	±0.016	±0.0047
17–20	0.5074	±0.0067	±0.0016	0.515	±0.010	±0.0027
20–25	0.5192	±0.0074	±0.0018	0.512	±0.011	±0.0033
25–40	0.6327	±0.0075	±0.00140	0.595	±0.013	±0.0018
40–100	0.551	±0.016	±0.0060	0.617	±0.037	±0.0059

Table D.1: The result of non-prompt to inclusive production fraction for each rapidity and p_T bin with systematical and statistical uncertainties.

Bibliography

[1] J. H. Christenson, J. W. Cronin, V. L. Fitch, and R. Turlay, "Evidence for the 2π decay of the k20 meson," *Phys. Rev. Lett.*, vol. 13, pp. 138–140, Jul 1964.

[2] D. H. Perkins, *Introduction to high energy physics*, vol. 2. Addison-Wesley Reading, Massachusetts, 1987.

[3] "Evidence for the spin-0 nature of the higgs boson using {ATLAS} data," *Physics Letters B*, vol. 726, no. 1–3, pp. 120 – 144, 2013.

[4] J. Beringer et al. (Particle Data Group), Phys. Rev. D86, 010001 (2012) and 2013 partial update for the 2014 edition.

[5] M. Gell-Mann, "A schematic model of baryons and mesons," *Physics Letters*, vol. 8, no. 3, pp. 214 – 215, 1964.

[6] G. Zweig, "An SU(3) model for strong interaction symmetry and its breaking. Version 2," pp. 22–101, 1964.

[7] R. Aaij *et al.*, "Observation of the resonant character of the $Z(4430)^-$ state," *Phys.Rev.Lett.*, vol. 112, p. 222002, 2014.

[8] E. Giusarma, R. de Putter, S. Ho, and O. Mena, "Constraints on neutrino masses from Planck and Galaxy Clustering data," *Phys.Rev.*, vol. D88, no. 6, p. 063515, 2013.

[9] P. A. M. Dirac, "Nobel Lecture: Theory of Electrons and Positrons." http://www.nobelprize.org/nobel_prizes/physics/laureates/1933/dirac-lecture.html. Accessed: 2014-05-21.

[10] T. D. Lee and C. N. Yang, "Question of parity conservation in weak interactions," *Phys. Rev.*, vol. 104, pp. 254–258, Oct 1956.

[11] C. S. Wu, E. Ambler, R. W. Hayward, D. D. Hoppes, and R. P. Hudson, "Experimental test of parity conservation in beta decay," *Phys. Rev.*, vol. 105, pp. 1413–1415, Feb 1957.

[12] N. Cabibbo, "Unitary symmetry and leptonic decays," *Phys. Rev. Lett.*, vol. 10, pp. 531–533, Jun 1963.

[13] S. L. Glashow, J. Iliopoulos, and L. Maiani, "Weak interactions with lepton-hadron symmetry," *Phys. Rev. D*, vol. 2, pp. 1285–1292, Oct 1970.

[14] L. Maiani, "The GIM Mechanism: origin, predictions and recent uses," pp. 3–16, 2013.

[15] F. Siebenhühner, "Determination of the qcd coupling constant from charmonium." http://theorie.ikp.physik.tu-darmstadt.de/nhc/pages/lectures/rhiseminar07-08/siebenhuehner.pdf. Accessed: 2014-05-21.

[16] T. Kawanai and S. Sasaki, "Heavy quarkonium potential from Bethe-Salpeter wave function on the lattice," *Phys.Rev.*, vol. D89, p. 054507, 2014.

[17] L. Y. Glozman, "Why is the Okubo-Zweig-Iizuka rule so strongly violated in J/ψ decays?," *Phys. Rev. D*, vol. 73, p. 017503, Jan 2006.

[18] W. Herr and B. Muratori, "Concept of luminosity," 2006.

[19] J. Karanicholas and J. Langlands, "W and z boson studies at lep." http://www.kudryavtsev.staff.shef.ac.uk/phy466/lep.pdf. Accessed: 2014-05-12.

[20] Accelerators and Technology Sector, "The CERN accelerator complex ." https://espace.cern.ch/acc-tec-sector/default.aspx. Accessed: 2014-05-12.

[21] CERN, "The accelerator complex." http://home.web.cern.ch/about/accelerators. Accessed: 2014-05-12.

[22] CERN Administrative Information Services, "Experiments at CERN." http://greybook.cern.ch/. Accessed: 2014-04-08.

[23] The ATLAS Collaboration at al. , "The atlas experiment at the cern large hadron collider," *Journal of Instrumentation*, vol. 3, no. 08, p. S08003, 2008.

[24] The ATLAS IBL collaboration, "Prototype ATLAS IBL modules using the FE-I4A front-end readout chip," *Journal of Instrumentation*, vol. 7, no. 11, p. P11010, 2012.

[25] Dr. Tobias Flick, "ATLAS Pixel Detector." http://www.atlas.uni-wuppertal.de/~flick/index.php/en/projects. Accessed: 2014-07-07.

[26] M. Capeans, G. Darbo, K. Einsweiller, M. Elsing, T. Flick, M. Garcia-Sciveres, C. Gemme, H. Pernegger, O. Rohne, and R. Vuillermet, "ATLAS Insertable B-Layer Technical Design Report," Tech. Rep. CERN-LHCC-2010-013. ATLAS-TDR-19, CERN, Geneva, Sep 2010.

[27] J. Wotschack, "ATLAS Muon Chamber Construction Parameters for CSC, MDT, and RPC chambers," Tech. Rep. ATL-MUON-PUB-2008-006. ATL-COM-MUON-2008-008, CERN, Geneva, Apr 2008.

[28] S. Tanaka, H. Ohshita, K. Ishii, H. Iwasaki, Y. Arataki, T. Bando, Y. Homma, M. Ishino, T. Kondo, T. Kobayashi, H. Kurashige, G. Mikenberg, Y. Miyazaki, Y. Nakagawa, H. Nanjo, M. Ikeno, M. Nozaki, A. Ochi, O. Sasaki, M. Shoa, T. Sugimoto, H. Takeda, T. Takeshita, and C. Yokoyama, "Development of mass-production technique of the ATLAS thin gap chamber in Japan," 2004.

[29] S. C. C. Ting, "Nobel Lecture: The Discovery of the J Particle: A Personal Recollection." http://www.nobelprize.org/nobel_prizes/physics/laureates/1976/ting-lecture.html. Accessed: 2014-05-21.

[30] B. Richter, "Nobel Lecture: From the Psi to Charm – The Experiments of 1975 and 1976." http://www.nobelprize.org/nobel_prizes/physics/laureates/1976/richter-lecture.html. Accessed: 2014-05-21.

[31] S. Godfrey, "Heavy Quarkonia." http://people.physics.carleton.ca/~godfrey/, 2007. Accessed: 2014-03-19.

[32] S. Eidelman, B. Heltsley, J. Hernandez-Rey, S. Navas, and C. Patrignani, "Developments in heavy quarkonium spectroscopy," 2012.

[33] R. Brun and F. Rademakers, "An Object Oriented Data Analysis Framework." ftp://root.cern.ch/root/laussanne.ps.gz. Accessed: 2014-05-21.

[34] T. Luminosity Group, "Preliminary Luminosity Determination in pp Collisions at sqrt(s) = 8 TeV using the ATLAS Detector in 2012," Tech. Rep. ATL-COM-LUM-2012-013, CERN, Geneva, Nov 2012.

[35] The ATLAS, "ATLAS Experiment, Public Results." https://twiki.cern.ch/twiki/bin/view/AtlasPublic/LuminosityPublicResults#Integrated_luminosity_summary_pl. Accessed: 2014-05-21.

[36] T. Colombo, "ATLAS TDAQ System Performance in 2012 Data Taking," Mar 2013.

[37] ATLAS B-physics, "ATLAS BPhysPublicResults." https://twiki.cern.ch/twiki/bin/view/AtlasPublic/BPhysPublicResults. Accessed: 2014-07-17.

[38] A. Farbin, "Atlas analysis model," *Journal of Physics: Conference Series*, vol. 119, no. 4, p. 042012, 2008.

[39] G. Aad *et al.*, "Expected Performance of the ATLAS Experiment - Detector, Trigger and Physics," 2009.

[40] T. Sjostrand, S. Mrenna, and P. Z. Skands, "A Brief Introduction to PYTHIA 8.1," *Comput.Phys.Commun.*, vol. 178, pp. 852–867, 2008.

[41] G. Aad, B. Abbott, J. Abdallah, A. A. Abdelalim, A. Abdesselam, O. Abdinov, B. Abi, M. Abolins, H. Abramowicz, H. Abreu, and et al., "The ATLAS Simulation Infrastructure," *European Physical Journal C*, vol. 70, pp. 823–874, Dec. 2010.

[42] G. Aad *et al.*, "Measurement of the differential cross-sections of inclusive, prompt and non-prompt J/ψ production in proton-proton collisions at $\sqrt{s} = 7$ TeV," *Nucl.Phys.*, vol. B850, pp. 387–444, 2011.

[43] The ROOT Team, "RooFit." http://root.cern.ch/drupal/content/roofit. Accessed: 2014-05-18.